



# Using fully variable valve control for cylinder-individual reference tracking with emission-optimal internal exhaust gas recirculation

Andyn Omanovic<sup>a,b,\*</sup>, Alvaro Detailler<sup>a,b</sup>, Patrik Soltic<sup>a</sup>, André Casal Kulzer<sup>c</sup>, Christopher Onder<sup>b</sup>

<sup>a</sup> Automotive Powertrain Technologies Laboratory, Empa Swiss Federal Laboratories for Materials Science and Technology, 8600 Dübendorf, Switzerland

<sup>b</sup> Institute for Dynamic Systems and Control, ETH Zurich, 8092 Zurich, Switzerland

<sup>c</sup> Institute for Automotive Engineering, University of Stuttgart, 70569 Stuttgart, Germany

## ARTICLE INFO

### Keywords:

Fully variable valve train  
Cycle-to-cycle based engine control  
Transient operation  
Internal EGR  
Online emission optimization

## ABSTRACT

A fully variable valve train significantly increases the degree of freedom of the control of internal combustion engines. Cylinder deactivation, thermal management, alternative combustion strategies, and minimized pumping losses are just a few examples enabled by freely adaptable intake and exhaust valve timings. This paper presents a method to achieve the accurate tracking of load trajectories under stoichiometric conditions. A feedback controller is designed with a mixed-sensitivity  $H_\infty$  synthesis method. The underlying system plant is modeled by a combination of a mean-value model of the cylinder-internal processes and a neural network to map the correlation between valve timings and cylinder charge. All experiments are conducted on a test bench with a spark-ignited engine equipped with an internally developed fully variable valve train called FlexWork. With this method, a mean absolute error of 0.07 bar in indicated mean pressure and of 0.009 in air-fuel equivalence ratio is achieved for the tracking of the reference trajectory. Furthermore, a cost function dependent online optimization of the internal exhaust gas recirculation is conducted without affecting the tracking performance of the load and stoichiometry. Depending on the parametrization of the cost function, nitrogen oxide or hydrocarbon pollutants can be reduced by up to 46% or 17%, respectively.

## 1. Introduction

Electric vehicles (EVs) are becoming more popular and penetrate some market segments faster than others (Fuinhas et al., 2021; Tchetchik, Zvi, Kaplan, & Blass, 2020). In 2021, the global market share of EVs lies below 9% (IEA, 2022). Today, the internal combustion engine (ICE) propels the majority of vehicles and contributes to about 23% of global greenhouse gas emissions (Hoeft, 2021). Segments such as long-range, heavy-duty, off-road and marine applications will in the near future still largely rely on chemical fuels (Horvath, Fasihi, & Breyer, 2018; Kalghatgi, 2018; Malaquias et al., 2019). To decarbonize these segments, renewable chemical energy carriers, such as hydrogen (Shadidi, Najafi, & Yusaf, 2021; Stepien, 2021), methane (Akansu, Dulger, Kahraman, & Veziroglu, 2004; Distaso et al., 2020), methanol (Sarikoç, 2021; Verhelst, Turner, Sileghem, & Vancoillie, 2019), ammonia (Cardoso et al., 2021; Dolan, Anderson, & Wallington, 2021), dimethyl ether (Awad et al., 2020; Awogbemi, Kallon, Onuh, & Aigbodion, 2021; Putrasari & Lim, 2021), or polyoxymethylene dimethyl ether (Pélerin,

Gaukel, Härtl, Jacob, & Wachtmeister, 2020; Popp et al., 2019), are required to substitute fossil oil based fuels. However, since manufacturing cost and availability of renewable energy sources are challenging, the decarbonization of fuel will be decision based rather on economical than on ecological considerations (Pischinger, 2019; Schemme et al., 2020; Towoju, 2021).

To effectively and immediately reduce global greenhouse gas emissions, not only the share of EVs must be increased, but the technological advancements of ICEs, such as electric hybridization and more efficient combustion strategies, must be further stimulated. Electric hybridization with charging capability is becoming a common standard in vehicles with an ICE since this approach promises a significant reduction of tailpipe emissions. However, if the hybrid vehicle is not charged as often as intended, the ICE is operated instead, which mitigates the expected reduction of emission. Thus, the further improvement of thermal efficiency and minimization of pollutants of ICEs will remain a crucial part of research and development efforts (Muratori et al., 2021; Song & Aaldering, 2019).

\* Corresponding author at: Automotive Powertrain Technologies Laboratory, Empa Swiss Federal Laboratories for Materials Science and Technology, 8600 Dübendorf, Switzerland.

E-mail address: [andyn.omanovic@empa.ch](mailto:andyn.omanovic@empa.ch) (A. Omanovic).

<https://doi.org/10.1016/j.conengprac.2023.105526>

Received 23 December 2022; Received in revised form 31 March 2023; Accepted 6 April 2023

Available online xxxx

0967-0661/© 2023 The Authors. Published by Elsevier Ltd. This is an open access article under the CC BY license (<http://creativecommons.org/licenses/by/4.0/>).

### 1.1. Current technologies

To increase the maximal thermal efficiency across the relevant operating range of an ICE, various methods can be applied. In this paper, these methods are grouped as follows:

**Propulsion system.** The reduction of friction and weight of moving parts generally improves the efficiency (Mafrić, 2020; Usman & Park, 2016). Downsizing and supercharging or electric boosting as well lead to a higher power density and increased efficiency (Alshammari, Alshammari, & Pesyridis, 2019; Emran et al., 2019; Xia et al., 2020; Xue & Rutledge, 2017). Electric start-stop system also eliminate idling losses (Dvadnenko, Arhun, Bogajevskiy, & Ponikarovska, 2018). Another advantage of an additional electric motor in the power train is the possibility of recuperating circulating energy and of shifting the operating point, which improves fuel economy (Benajes, García, Monsalve-Serrano, & Martínez-Boggio, 2019; García, Monsalve-Serrano, Martínez-Boggio, & Wittek, 2020).

**Combustion.** The thermal efficiency is improved by increasing the compression ratio, which on the other hand is restricted by knock limitations in the case of spark-ignited engines. However, the risk of knock can be reduced by methods such as direct injection or water injection (Bozza, Bellis, & Teodosio, 2016; Hoppe, Thewes, Baumgarten, & Dohmen, 2015; Zhu et al., 2019). Furthermore, reducing wall heat losses, for instance by thermal swing coating of combustion chamber surfaces, positively affects the thermal efficiency (Caputo et al., 2019; Saputo et al., 2020). Also lean combustion concepts with diffusion flame, pre-chamber, or pilot ignition are helpful to improve efficiency (Alvarez, Couto, Roso, Thiriet, & Valle, 2018; Zurbriggen, Hutter, & Onder, 2016). Thereby, an efficiency above 45% is achievable for passenger car sized engines (Soltic, Hilfiker, & Hänggi, 2019). However, such lean spark- and compression-ignited concepts require an adequate exhaust aftertreatment system.

**Gas exchange.** Currently, the gas exchange of an ICE is being improved with various mechanisms acting on the valves such as phase and lift controllers or switching cam profiles. Nonetheless, these systems can be optimized only for a certain operating range. The full potential of a gas exchange optimization can only be exploited by a fully variable valve train (FVVT). In the following, the focus lies on spark-ignited engine systems. However, most of these concepts are also applicable to compression-ignited engine systems. The pumping losses occurring in part-load operation can be minimized by setting the cylinder charge with appropriate valve timings instead of with the conventional throttle (Balmelli, Zsiga, Merotto, & Soltic, 2020). For instance, with Miller valve timings (Judith, Neher, Kettner, Schwarz, & Klaisle, 2020) the intake valve closes early and with Atkinson valve timings (Oh et al., 2018) the intake valve closes late. Both approaches are not just minimizing pumping losses, but they also increase the thermal efficiency due to an extended expansion stroke relative to the compression stroke (Zsiga, Omanovic, Soltic, & Schneider, 2019b). Furthermore, the variable compression ratio in combination with external exhaust gas recirculation (EGR) allows the reduction of the formation of nitrogen oxides ( $\text{NO}_x$ ) and hydrocarbons (HC) while the thermal efficiency improves (Feng, Wei, & Pan, 2018). As efficiency increases with load, cylinder deactivation is advantageous in part-load operation since it disables a certain number of cylinders while the remaining cylinders remain operational at an increased load (Kuruppu, Pesiridis, & Rajoo, 2014; Leone & Pozar, 2001; Ritzmann, Zsiga, Peterhans, & Onder, 2020; Zhao, Xi, Wang, & Wang, 2018).

Research into FVVTs has focused primarily on accurately determining the expected improvements in efficiency and examining novel control strategies, such as cylinder deactivation. Studies that have gathered empirical data from prototype systems to validate theoretical studies almost exclusively use steady-state measurements, but do not analyze

transient operation (Fernandes, Pimenta, Rodrigues, de Souza Montemor, & Barros, 2016; Flierl, Lauer, Breuer, & Hannibal, 2012). Nowadays, model predictive control algorithms are often used and studied to optimize transient operation (Gosala et al., 2021; Hänggi, Frey, van Dooren, Diehl, & Onder, 2022; Koli, Egan, Zhu, & Prucka, 2023; Yang et al., 2019; Yin, Turesson, Tunestal, & Johansson, 2020). Although these studies are conducted on engine systems with variable valve timing, the valve actuation is still based on a camshaft and is therefore not fully variable. Of the few studies done on the dynamic control of FVVT systems, the most extensive investigation of which the authors are currently aware, Pischinger, Salber, van der Staay, Baumgarten, and Kemper (2000), outlines various high-level operating modes to achieve load control and variable internal EGR. However, a general system-theoretic design of a control system for FVVT applications is not discussed. Several variable valve concepts have been introduced by industry. The most advanced include BMW's valvetronic system (Unger, Schwarz, Schneider, & Koch, 2008), the MultiAir system by Fiat Powertrain Technologies (Haas & Rauch, 2010), the intelligent variable valve timing and lift control system i-VTEC by Honda, and the continuous variable valve duration system CVVD by Hyundai (Lou & Zhu, 2020). For commercial reasons, the control system design methods for these systems are not scientifically published. However, none of these systems are fully variable as all systems still rely on a mechanical cam which limits the crank angle range in which valves may be opened. Overall, no significant previous research has been found that is relevant to the objective of this paper. A novel control synthesis method to enable transient operation of a FVVT system is thus presented here.

### 1.2. Objective

The development of an FVVT for use in internal combustion engines has been investigated in various forms over the last decades (Fernandes et al., 2016; Flierl et al., 2012; Haas & Rauch, 2010; Maas, Neukirchner, Dingel, & Predelli, 2004; Pischinger et al., 2000; Unger et al., 2008). Conceptually, the introduction of an FVVT significantly increases the number of degrees of freedom in the control of each combustion cycle. However, to make the most of the flexibility offered by a variable valve train system, a novel control design is required. Therefore, the objective in this paper is to synthesize a controller to allow the dynamic operation of an internally developed fully variable valve train system called FlexWork (Zsiga, Omanovic, Soltic, & Schneider, 2019a). The FlexWork system operates without a cam, allowing a greater flexibility than current industrialized systems. Previous work shows significant efficiency improvements in steady-state operation enabled by FlexWork, such as an x-stroke operation (Omanovic, Zsiga, Soltic, & Onder, 2021) and cylinder deactivation (Zsiga et al., 2019a).

The control system presented in this paper contributes to the goal of following trajectories of the mean indicated pressure  $p_{mi}$  as accurately as possible with a desired air-fuel equivalence ratio  $\lambda$  of 1 and an emission-optimal EGR rate. The mean indicated pressure is chosen over torque as the tracking objective since it can be evaluated for each cylinder individually. By applying Miller valve timings and a wide open throttle, the desired charge is adaptable for each cylinder and each combustion event individually. Furthermore, an FVVT allows to adapt not only the intake valves but also the exhaust valves on a cycle-to-cycle basis. Thus, the amount of EGR can be set almost arbitrarily for every cycle as long as it does not prevent a charge of fresh air/fuel mixture sufficient for the requested load and does not exceed certain maximal rates where an ignition of the mixture is not reliably possible. The  $p_{mi}$  value of the trajectory is fed into a cost function which estimates  $\text{NO}_x$  and HC emissions. The optimization of this cost function which depends on a weighting parameter leads to a required EGR rate, which is achieved by setting the valve timings at the gas exchange top dead center accordingly. The controller is designed to consider the changes in EGR rate such that  $p_{mi}$  and  $\lambda$  are not affected.

**Table 1**  
Details of the equipment used on the engine test bench.

Equipment	Details
Dynamometer	Dynas3 LI250 (Horiba)
Engine basis	EA111 (Volkswagen)
Displacement	1.4 L, 4 cylinders
Bore/stroke	76.5 mm/75.6 mm
Compression ratio	10
Fuel	Port-injected CNG
Injectors	NGI2 (Bosch)
Valve train	FlexWork (internally developed)
Valve lift measurement	Linear encoders (Elgo Electronics)
Valve lift	1-9 mm, exhaust and intake
Valve timing	individual on all valve pairs
Engine control unit	MicroAutoBoxII (dSPACE)
Stoichiometry sensors	Wide-range, LSU 4.9 (Bosch)
In-cylinder piezoelectric pressure sensors	Type 6061B (Kistler)
Fuel flow measurement	RHM015 (Rheonik)
Air flow measurement	Sensyflow P (ABB)
Torque transducer	T40 (HBM)
Flywheel	Standard dual mass
Gearbox	None
Exhaust gas analyzer	Mexa-One (Horiba)

### 1.3. Structure

The paper at hand is structured as follows: In Section 2 the engine test bench used is presented. Section 3 discusses the formulation, parameter identification, and validation of a cylinder-specific mean-value engine system model, followed by the analysis and development of a control synthesis technique for the fully variable valve train engine system. The results of the trajectory tracking with this controller and the discussion are presented in Section 4. Section 5 contains the conclusion and the outlook.

## 2. Setup of the engine test bench

In the first part of this section, the base engine used and the test bench equipment are presented. In the second part, the functionality principle of the internally developed FVVT is explained.

### 2.1. Engine test bench

The base engine for this project is a 1.4 L spark-ignited Volkswagen engine of the type EA111 whose camshaft driven valve train is replaced by an electro-hydraulic actuated FVVT called FlexWork (Zsiga et al., 2019a). While the original engine supercharging setup consists of a mechanical compressor and a turbocharger, for simplicity, the setup is reduced to the mechanical compressor only. The operation of a turbocharger can be emulated with an additional flap to create back pressure in the exhaust. The engine control software developed in-house runs on a MicroAutoBoxII, a rapid prototyping system by dSPACE. All cylinders are equipped with pressure transducers such that the center of combustion can be evaluated and controlled in real-time to remain at an efficient optimal value of 8° crank angle (CA) after the top dead center (TDC). In each exhaust manifold runner a wide-band lambda sensor is installed to ensure a stoichiometric combustion by cylinder-individual feedback control. Compressed natural gas (CNG) is used as a fuel, which is port-injected. The fuel mass flow is measured with a Coriolis sensor and the air mass flow is measured with a hot film anemometer. The exhaust gases are extracted directly after the exhaust manifold and are analyzed in the motor exhaust gas analyzer of the type Mexa-One. All emission-related results stem from raw emission measurements. The aftertreatment system is not considered here. Details of the equipment used are listed in Table 1.

### 2.2. FlexWork – The fully variable valve train

FlexWork is a cam-less, electro-hydraulic, fully variable valve train. Valve lift and valve timings can be selected independently and freely on the intake and exhaust sides. To compete with current cam-based systems, besides a maximal degree of freedom, an FVVT must offer a low energy demand and minimal complexity in terms of design and operation. This is achieved in the FlexWork valve train with a specific arrangement of check valves, which offer the following advantages:

- The maximal valve lift is maintained without any additional control action.
- During the closing procedure, the working fluid is automatically recuperated into the high-pressure reservoir.
- Since no control input is required at high flow rates, relatively slow actuators are sufficient.
- During the valve motion, no low-level electronic feedback control is required.

Furthermore, the hydraulic fluid is a 1:1 mixture of water and ethylene glycol, as it is often used as an engine coolant. This mixture possesses a higher stiffness compared to hydraulic oils, which causes lower capacitive losses during the operation of the FVVT. The energy demand of FlexWork is comparable to the operation of a camshaft-driven valve train. Additionally, FlexWork allows for a completely oil-free cylinder head design, which makes it possible to reduce additives in the engine oil since high surface pressures at the cam lobes do not occur.

The working principle of FlexWork is based on an asymmetric hydraulic pendulum that can be described as a mass-spring-system (Schechter & Levin, 1996). Fig. 1 shows the core components of the FlexWork mass-spring system on the left-hand side as a schematic and on the right-hand side as a computer-aided design (CAD) rendering, which depicts one intake-side module cut in its half-plane. The hydraulic circuit comprising check valves and the detailed assembly of the hydraulic valve are not shown. A solenoid (a) actuates a three-way, two-positions valve (b). When actuated, the hydraulic valve enables the fluid in a high-pressure reservoir (c) to apply a hydraulic force on the working piston (e). As a consequence, two gas exchange valves (h) connected over a valve bridge (f) are opened and the gas exchange valve springs (g) are compressed. During this opening process, the system overshoots its equilibrium point and fluid is replenished. At the turn-over point, i.e. at the maximal valve lift, the fluid is trapped by check valves and the gas exchange valves cannot return to the equilibrium point. As a consequence of the energy stored in the springs (g), the pressure of the hydraulic fluid exceeds the level of the high-pressure reservoir (c). With the deactivation of the solenoid (a) the recuperation of the hydraulic fluid into the high-pressure reservoir (c) is enabled. The remaining fluid is then drained to the low-pressure reservoir (d) until the gas exchange valve springs reach their initial length, i.e. until the gas exchange valves are fully closed.

The equation

$$T_{\text{valve}} = \pi \cdot \sqrt{\frac{M_{\text{comp}}}{k_{\text{spring}}}} \quad (1)$$

expresses the duration of half a period which such a mass-spring system excites. This is the time the gas exchange valves require to go from zero lift to the final lift, as well as the time required for the closing procedure. It depends on  $k_{\text{spring}}$ , the cumulative stiffness of both gas exchange valve springs (g), and the mass  $M_{\text{comp}}$  of all moving components, i.e. the mass of the working piston (e), the valve bridge (f), the gas exchange valves (h), and approximately one third of the mass of the springs (g). Once the system design is fixed and thus the value of  $T_{\text{valve}}$  is known, the hydraulic circuit is designed such that the recuperation procedure, which takes  $T_{\text{valve}}$  seconds, can be completed before the remaining fluid is purged to the low-pressure reservoir.

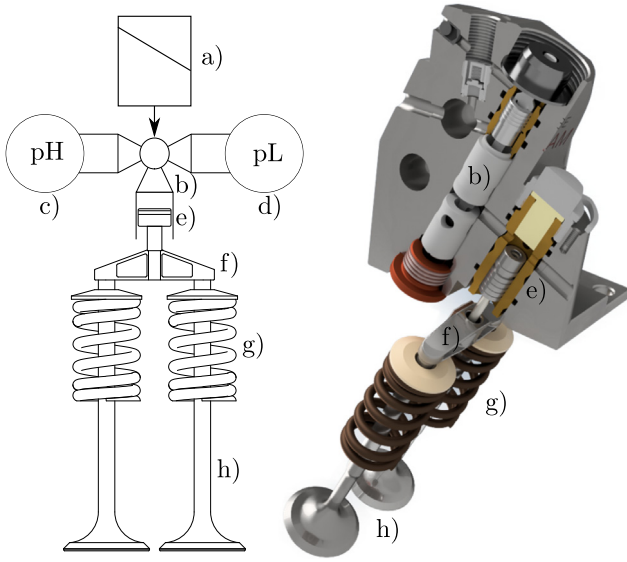


**Fig. 1.** A schematic of the hydraulic core components and a CAD rendering of the fully variable valve train mass-spring system named FlexWork with the following components: (a) solenoid, (b) hydraulic 3/2-way valve, (c) high-pressure reservoir, (d) low-pressure reservoir, (e) working piston, (f) gas exchange valve bridge, (g) gas exchange valve springs, and (h) gas exchange valves.

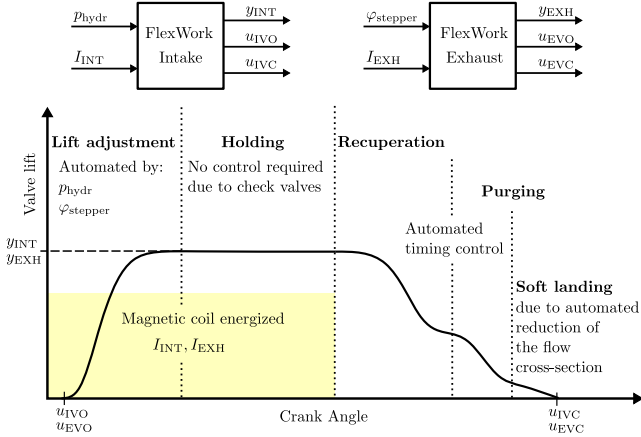


**Fig. 2.** A schematic representation of the control circuits and the various stages of a gas exchange valve lift of the FlexWork system.

**Fig. 2** shows in the lower part the various stages during a single gas exchange valve lift and in the upper part the individual control circuits of the intake and the exhaust side of the FlexWork system. The only difference between the intake and exhaust sides are the lift adjustment mechanisms. For the former, the lift  $y_{INT}$  is determined by the hydraulic pressure level  $p_{hydr}$ . For the latter, the lift  $y_{EXH}$  is given by a slanted edge which is set by a stepper motor  $\varphi_{stepper}$ . The slanted edge and the increased hydraulic pressure enable the exhaust valves to open against high cylinder pressures without overshooting. The current system is set up with a maximum hydraulic supply pressure of 200 bar. This allows the exhaust valves to open approximately 60°CA after the ignition TDC. The opening and closing instances of the intake and exhaust valves,  $u_{IVO}$ ,  $u_{IVC}$ ,  $u_{EVO}$ ,  $u_{EVC}$ , are determined by the current duration  $I_{INT}$  and  $I_{EXH}$ , respectively. During  $I_{INT/EXH}$  the solenoid is energized and, hence, the valves are kept open. The termination of the current supply initializes the closing process which begins with the recuperation procedure. Subsequently, the remaining fluid is purged

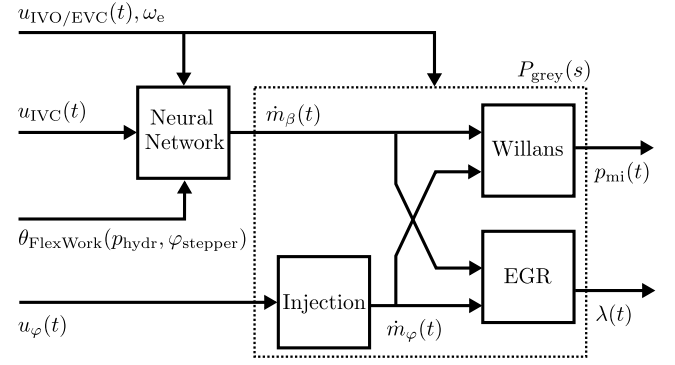


**Fig. 3.** A schematic overview of the overall engine model structure.

into the low-pressure reservoir. Finally, to avoid wear, shortly before landing the gas exchange valves are decelerated with a fixed reduction of the flow cross-section. Details on each stage of the valve lift are published in [Zsiga et al. \(2019b\)](#).

### 3. Mean value model and controller synthesis

In this section, the choice for the development of a mean-value model underpinning the control design and the  $\mathcal{H}_\infty$  method of controller synthesis are discussed. To minimize the dimensionality of the required mapping, the following restrictions are applied:

- Constant engine speed of  $\omega_e = 2000$  rev/min.
- The engine load is set by Miller valve timings, i.e.  $0^\circ < u_{IVC} < 180^\circ$  after gas exchange TDC, while the throttle is always wide open.
- $y_{INT}$  is kept constant at approximately 2.2 mm.
- No valve overlap, i.e. intake and exhaust valves are never simultaneously open and  $u_{IVO} = u_{EVC}$ .
- For a fuel optimal expansion,  $u_{EVO}$  equals  $170^\circ$  after ignition TDC for all operating points.
- All sub-models are identified only under stoichiometric engine operation.

The model assumes a stoichiometric operation of the engine. Deviations from such operation are considered in the controller synthesis.

#### 3.1. Model setup

To describe the engine system, the model is split into a neural network and a mean-value model  $P_{grey}(s)$  as shown in **Fig. 3**. The neural network describes the expanded actuation capabilities that the FlexWork system offers and takes  $u_{IVO/EVC}(t)$ ,  $\omega_e$ ,  $u_{IVC}(t)$  and  $\theta_{FlexWork}$  as inputs. Here,  $\theta_{FlexWork}$  contains parameters of the valve train such as  $p_{hydr}$  and  $\varphi_{stepper}$ . The output of the neural network is the inducted air mass flow rate  $\dot{m}_\beta(t)$ . The mean-value model  $P_{grey}(s)$  models the remaining physical processes taking place in the engine. Its inputs are  $u_{IVO/EVC}(t)$ ,  $\omega_e$ ,  $\dot{m}_\beta(t)$  and the injection duration  $u_\varphi(t)$ . The cylinder-specific mean indicated pressure,  $p_{mi}(t)$ , and the air-fuel equivalence ratio,  $\lambda(t)$ , comprise the model outputs. Three main sub-models make up the mean-value model: an injector model, a steady-state model of the exhaust gas recirculation (EGR) rate, and a Willans approximation of the engine's  $p_{mi}(t)$  and efficiency characteristics. This approach allows the nonlinear FlexWork system behavior to be described while maintaining the ability to use first-principle models to describe the remaining processes taking place in the engine system. In addition, this structure enables a controller to be developed for  $P_{grey}(s)$  separately, allowing the FlexWork system behavior to be isolated.



**Neural network for the FlexWork system.** The additional degrees of freedom to control the combustion process enabled by the FlexWork valve train all affect the volumetric efficiency of the engine system. Furthermore, the relation between the inputs to the FlexWork system and the inducted air mass flow rate into the cylinder,  $\dot{m}_\beta(t)$ , is highly nonlinear. These effects could be captured by computational fluid dynamics simulations. However, as a more computationally efficient approach, the volumetric efficiency is represented by a neural network, i.e. a multi-layer perceptron regressor ([scikit documentation page of MLPRegressor](#), 2022). The architecture consists of one hidden layer with three neurons and a rectified linear unit activation function. The target of the neural network is  $\dot{m}_\beta$ . The choice of features depends on the desired accuracy. A full neural network has the following features:

- The IVC instance,  $u_{IVC}$ ,
- the cylinder volume at the EVC instance, i.e.  $V_{EVC}$ ,
- the lift of the exhaust valves expressed by  $\varphi_{stepper}$ ,
- and the pressure in the intake manifold  $p_{IM}$  relative to the environment.

This setup allows a high accuracy of the estimation. However,  $p_{IM}$  is a sensor output which underlies noise and physical delays. Thus, at the cost of a marginally worse accuracy but for a more robust output, a reduced neural network is introduced. It has the same architecture as the full neural network, but does not comprise  $p_{IM}$  in its features. To allow the neural network to be used in the engine control system discussed in Section 4, the neural network is not inverted, as it is done with  $P_{grey(s)}$  to form a feedforward controller. Rather, the network is retrained with  $\dot{m}_\beta$  becoming a feature and  $u_{IVC}$  the target. This approach is feasible since for a given set of features and the boundary condition  $u_{IVO} < u_{IVC} \leq 180^\circ \text{CA}$  after TDC, for each  $\dot{m}_\beta$  exists a unique  $u_{IVC}$ .

**Grey box mean-value model.** Once the inducted air charge mass flow rate has been calculated, this quantity is used in a cylinder-specific mean-value model. For each cylinder and for a given  $\omega_e$ , this model takes inlet valve opening/exhaust valve closing timing,  $u_{IVO/EVC}(t)$ , the inducted air mass flow  $\dot{m}_\beta(t)$ , and the injection duration  $u_\varphi(t)$  as inputs. Subsequently, it calculates the cylinder-specific indicated mean effective pressure  $p_{mi}(t)$  and the air–fuel equivalence ratio  $\lambda(t)$ .

The main assumption underlying this mean-value model is that physical quantities (e.g. mass flows,  $p_{mi}(t)$ ) are assumed to be continuous. This neglects the inherent discrete and reciprocating behavior of internal combustion engines, which is only a valid assumption at time scales greater than that of the discrete combustion behavior ([Guzzella & Onder, 2004](#)). Given the delays present in the input–output behavior of engine systems and the fundamental limitations this poses to feedback control performance ([Postlethwaite, 1996](#)), this choice of model does not limit the feedback control performance achievable. More detailed process models are therefore of limited value for feedback control synthesis while adding significant complexity. It is for this reason that dynamic sensor models, such as lambda sensors in the exhaust manifold, can safely be neglected, and (discrete)  $P_{grey(s)}$  model quantities, such as  $u_\varphi(t)$  and  $p_{mi}(t)$ , are assumed to be continuous.

**Injection model.** A standard injection model for gaseous fuels is utilized to relate the injection duration  $u_\varphi(t)$  in  $^\circ\text{CA}$  to the average flow rate  $\dot{m}_\varphi(t)$  at which fuel is injected. Under the assumptions of constant electrical excitation characteristics of the injection solenoid, a minimum fuel injection amount such that a steady-state injection rate  $\dot{m}_{\varphi,ss}$  is achieved temporarily during the combustion cycle and choked isentropic valve behavior, as well as general mean-value behavior, there exists an affine relationship between the average injected fuel mass per cylinder per combustion cycle,  $m_\varphi(t)$ , and the injection duration,  $u_\varphi(t)$  ([Cammalleri, Pipitone, Beccari, & Genchi, 2013](#); [Onofrio, Napolitano, Abagnale, Guido, & Beatrice, 2021](#)). This is described as

$$\dot{m}_{\varphi,ss} = c_d \cdot A \cdot \frac{p_\varphi(t)}{\sqrt{R_\varphi \cdot \vartheta_\varphi}} \sqrt{\kappa \cdot \left(\frac{2}{\kappa+1}\right)^{\left(\frac{\kappa+1}{\kappa-1}\right)}}, \quad (2)$$

$$m_\varphi(t) = \left( \frac{u_\varphi(t)}{180^\circ} \frac{\pi}{\omega_e(t)} - \tau_{inj} \right) \cdot \dot{m}_{\varphi,ss}. \quad (3)$$

The mean fuel flow rate, under the mean-value assumption, then follows as  $\dot{m}_\varphi(t) = m_\varphi(t) \frac{\omega_e}{4\pi}$ . The variables  $c_d$  and  $\tau_{inj}$  are two constants that can be identified for each cylinder using linear regression on steady-state fuel injection measurements.

**EGR model.** The FlexWork system enables the adjustment of the exhaust valves such that an arbitrary EGR rate can be achieved. The minimal EGR rate results from  $u_{IVO/EVC}(t)$  being set to the TDC. Note that through scavenging, i.e. the simultaneous opening of the exhaust and the intake valves while the pressure in the intake is higher than in the exhaust, the amount of residual gas could be further decreased. However, to allow for the calculation of the composition inside the cylinder with simple geometrical approaches, we refrain from scavenging methods. Thus, during all experiments conducted  $u_{IVO} = u_{EVC} = u_{IVO/EVC}$ . By setting  $u_{IVO/EVC}$  later than the TDC, a variable amount of exhaust gases can be reinducted from the exhaust manifold and be trapped in the combustion chamber. The lift of the exhaust valves can be sufficiently decreased such that the piston can pass TDC while these valves are kept open. The downward motion of the piston causes a reinduction of the afore discharged exhaust gases. The term used for this concept is internal exhaust gas recirculation (EGR). Unlike conventional EGR systems, FlexWork allows adapting the internal recirculation rate on a cycle-to-cycle basis. Furthermore, since with internal EGR the temperature of the reinducted gas is much higher than with external EGR, the indicated efficiency of the combustion remains basically constant. Modeling this phenomenon and its effect on the composition of the air–fuel mixture present in the cylinder therefore requires a recursive model formulation. For this purpose a EGR model which assumes thermal equilibrium is used in which the mean total inducted mass in one cylinder per combustion cycle,  $m_m(t)$ , and the mean total recirculated exhaust gas mass in one cylinder per combustion cycle,  $m_{EGR}(t)$ , are modeled as mixing homogeneously and adiabatically during the intake stroke.

The value of  $\dot{m}_m(t)$  and the composition of the inducted gases,  $\lambda_m(t)$ , are calculated using the mass flow rates  $\dot{m}_\beta(t)$  and  $\dot{m}_\varphi(t)$  from the aforementioned neural network and injection model. Under the assumption that the mean fuel flow rate and valve timings lead to a stoichiometric mixture and assuming that the air and fuel mass flows mix homogeneously,  $\lambda_m(t)$  and  $\dot{m}_m(t)$  may be described as

$$\lambda_m(t) = \frac{1}{\sigma_0} \frac{\dot{m}_\beta(t)}{\dot{m}_\varphi(t)}, \quad (4)$$

$$\dot{m}_m(t) = \dot{m}_\beta(t) + \dot{m}_\varphi(t), \quad (5)$$

where  $\sigma_0$  represents the fuel ratio normalization constant. Under the assumption that the closed-loop model inputs result in an approximate stoichiometric plant operation, the relations given by (4) and (5) are valid. Any remaining errors are treated as model mismatch errors and are explicitly accounted for in the controller synthesis.

The quantity of recirculated exhaust gases is calculated via the ideal gas law. Here, the cylinder geometry is assumed to be known, the exhaust manifold pressure assumed constant and the exhaust gas composition assumed stoichiometric. The temperature of the exhaust gases at time  $t$ ,  $\vartheta_{exh}(t)$ , is found by identifying a bilinear relationship from the cylinder-specific  $p_{mi}$  value and the rotational speed  $\omega_e$  to the exhaust gas temperature  $\vartheta_{exh}(t)$  under steady-state conditions. The composition of the reinducted exhaust gases is found by using the air–fuel ratio corresponding to the relevant combustion having previously taken place  $\tau_{IEG} - \tau_{IPS} = \frac{3\pi}{\omega_e} - \frac{2\pi}{\omega_e} = \frac{\pi}{\omega_e}$  seconds ago, in accordance with the overall mean value assumptions. This results in the following recursive formulation:

$$\vartheta_{exh}(t) = f(p_{mi}(t - (\tau_{IEG} - \tau_{IPS})), \omega_e), \quad (6)$$

$$m_{EGR}(t) = \frac{p_{em} \cdot V_{EVC}(t)}{R_{exh} \cdot \vartheta_{exh}(t)}, \quad (7)$$

$$m_m(t) = \dot{m}_m(t) \frac{4 \cdot \pi}{\omega_e}, \quad (8)$$

$$\lambda(t) = \frac{m_m(t) \cdot \lambda_m(t - \tau_{IEG}) + m_{EGR}(t) \cdot \lambda(t - \tau_{IEG})}{m_m(t) + m_{EGR}(t)}, \quad (9)$$

Here, the variables  $V_{EVC}(t)$ ,  $R_{exh}$ , and  $\lambda(t)$  denote the cylinder volume at the instant the exhaust valve closes, the specific gas constant of stoichiometric exhaust gases, and the total normalized air–fuel ratio of the gases in the combustion chamber at inlet valve closing, respectively.

**Willans approximation.** Finally, to establish the mean effective pressure  $p_{me}(t)$ , the thermodynamic efficiency of the system is captured by means of a Willans model (Guzzella & Onder, 2004; Guzzella & Sciarretta, 2013). In this model, the output,  $p_{me}(t)$ , is calculated by relating the fuel mean effective pressure,  $p_{mq}(t) = \frac{\dot{m}_\phi(t) \cdot H_{L,CNG}}{V_{d,cyl}(t)}$ , a property of the charge in the cylinder as the inlet valve closes at time  $t$ , to the torque produced by one cylinder,  $T_{cyl}(t)$ , expressed as,  $p_{me}(t) = \frac{T_{cyl}(t) \cdot 4 \cdot \pi}{V_{d,cyl}(t)}$ ,  $\tau_{IPS}$  seconds later, as

$$p_{me}(t) = e(t - \tau_{IPS}) \cdot p_{mq}(t - \tau_{IPS}) + p_{meOf}(t) + p_{meOg}(t) \quad (10)$$

$$e(t) = e_\lambda(t) \cdot e_{nom}(t). \quad (11)$$

Here, the variable  $H_{L,CNG}$  represents the lower heating value of the CNG fuel. The quantity  $e(t)$  represents the indicated efficiency of the combustion. It consists of a nominal value under stoichiometric operation,  $e_{nom}(t)$ , as well as a multiplicative factor taking into account the effect of non-stoichiometric combustion,  $e_\lambda(t)$ . The variable  $e_{nom}(t)$  is fitted over  $\dot{m}_\beta(t)$  and  $u_{IVO/EVC}(t)$ , while  $e_\lambda(t)$  is normalized with respect to a stoichiometric mixture and directly dependent on the air–fuel equivalence ratio of the gases present in the cylinder,  $\lambda(t)$ . This factor is of great importance to correctly model the cross couplings present in the engine system. The remaining terms  $p_{meOf}(t)$  and  $p_{meOg}(t)$  represent the mechanical friction in the engine system and the pumping losses of the gases, respectively, that result over the course of the combustion cycle. All of the above parameters are identified and/or calculated from measurements in steady-state operation.

**Model validation results.** The accuracy of the injection, the FlexWork neural network and the Willans approximation sub-models were identified by calculating the coefficient of determination ( $R^2$ ) and root-mean-square error (RMSE) values over the specified operating range. The accuracy of the EGR sub-model cannot be validated with steady-state measurements as  $\lambda(t)$  asymptotically approaches  $\lambda_m(t)$  in steady-state. The provided values are averaged over all cylinders.

Comparing the measured fuel mass flow rate to that predicted by the injector model,  $R^2$  and RMSE values of 0.997 and 3.28  $\frac{mg}{s}$  are found, respectively. The full neural network achieves an  $R^2$  score of 0.985 and an RMSE value of 2.40°. The reduced neural network achieves an  $R^2$  score of 0.979 and an RMSE value of 2.89°. Finally, as the  $p_{mi}$  value of the Willans approximation is utilized in the control design, the calculated indicated efficiency under stoichiometric conditions is compared to that predicted by the model. The Willans approximation achieves  $R^2$  and RMSE values of 0.972 and 0.22 %, respectively.

### 3.2. Controller synthesis

Based on the plant model shown in Fig. 3, an overall controller consisting of a feedforward controller  $K_{ff}(s)$ , a feedback controller  $K_{fb}(s)$ , and an inverted neural network is designed, as shown in Fig. 4. The synthesis of  $K_{ff}(s)$  is based on the plant inversion of  $P_{grey}(s)$ . Given the strong cross-coupling effects present between the input and output channels of the model,  $K_{fb}(s)$  is a MIMO feedback controller synthesized via  $H_\infty$  synthesis. The ‘inverted’ neural network is not a direct inversion of the neural network presented above but trained anew such that  $u_{IVC}$  becomes the target of the estimation instead of  $\dot{m}_\beta$ .

The structure shown in Fig. 4 has the clear advantage of allowing linear control design techniques to be used to control the nonlinear system since the highly nonlinear relation between valve timings and air

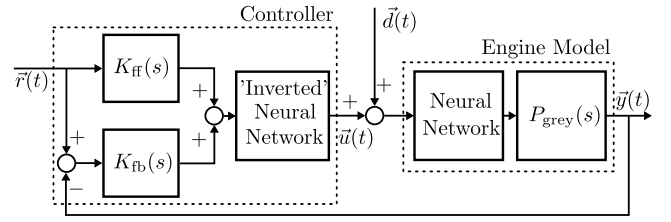


Fig. 4. A schematic overview of the overall controller structure, consisting of a feedforward controller  $K_{ff}(s)$ , a feedback controller  $K_{fb}(s)$ , and an ‘inverted’ neural network.

flow is treated in isolation in the neural network. From this perspective, the neural network may be viewed as enabling a reparametrization to a more suitable and linear domain for control design. In addition, the  $H_\infty$  synthesis method explicitly allows the specific model uncertainty arising from the model inversion and simplifying assumptions to be incorporated in the synthesis process.

**Linear control design.** The linear control elements are synthesized under the assumption that the neural network achieves the desired effect of model inversion. Hence, the plant for controller synthesis is  $P_{grey}$  shown in Fig. 3 which receives the cylinder-specific inducted air mass flow rate  $\dot{m}_\beta$  and the injection duration  $u_\phi$  as inputs.

The feedforward controller  $K_{ff}(s)$  is obtained via the inversion of a linearized minimum-phase model of  $P_{grey}$ . This inversion implies that all delays present in the model formulation are set to 0 and that steady-state inputs leading to stoichiometric combustion at a set  $p_{mi}$  value are found. Using the *linearize* function available as part of the Simulink Control Design toolbox in MATLAB (Mathworks, 2022), a linearized model may be obtained numerically. This model is finally inverted to form  $K_{ff}(s)$ .

The feedback controller  $K_{fb}(s)$  is constructed with a mixed-sensitivity  $H_\infty$  synthesis method. In principle, this method of controller synthesis finds an optimal controller that minimizes the induced 2-norm of the system between a set of vector-valued inputs and outputs. The control designer is able to express the importance of particular input or output channels or frequency ranges by introducing suitable, frequency-dependent weights on the input and output channels. To apply this method to the case at hand, first,  $P_{grey}$  is linearized around a suitable operating point. An operating point is found in steady state by using the boundary conditions  $\dot{m}_\beta(t) = 0.002 \text{ kg/s}$ ,  $\lambda(t) = 1, \forall t$ . Using the aforementioned numerical linearization techniques available in MATLAB, a suitable linear model of the grey-box formulation is found. Next, before application of the  $H_\infty$  methods, the resulting internal delays of the model that capture the delay between induction and exhaust of quantities which are physically ‘stored’ in the combustion chamber, are approximated via the use of first-order Padé elements. This process ensures that the transfer function, now referred to as  $P(s)$ , is in a form with a finite number of pole-zeros. Next, the structure of the  $H_\infty$  problem is set up by selecting the inputs and outputs of the optimization problem. Given the primary role of the feedback controller of disturbance rejection under the assumption of feedforward control inputs, the model inputs for the optimization problem are chosen to be disturbance inputs acting on the controller output. This setup encapsulates the combined effect of all previous model uncertainties. The performance output is selected to be a stacked vector of the controller inputs and deviations from the desired model outputs,  $\vec{v}(t)$ . This formulation is represented schematically in Fig. 5.

The chosen generalized plant formulation of  $\tilde{P}(s)$  allows requirements to be placed directly on the stacked vector of the input complementary sensitivity function,  $T_1(s) = (I + K(s) \cdot P(s))^{-1}$ , and the output sensitivity function times the plant,  $S_O(s) = (I + P(s) \cdot K(s))^{-1} \cdot P(s)$ . This formulation allows to specify the frequency up to which a good control performance is required and the maximum control frequency,

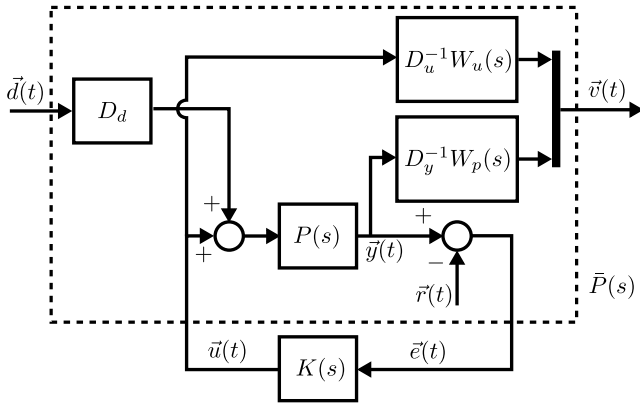


Fig. 5. A schematic overview of the generalized plant  $\bar{P}(s)$  used in the  $H_\infty$  design process.

which is limited by the delays present in the plant model as well as by the neglected discrete event behavior.

Once the system has been brought to this general form, static normalizations are performed on the model inputs and outputs in order to correctly be able to compare differing physical quantities against one another. Scaling matrices  $D_d = \text{diag}(2.5e^{-4}, 5)$ ,  $D_u = \text{diag}(5e^{-4}, 10)$ , and  $D_y = \text{diag}(0.5, 0.05)$  are used for normalization purposes of  $d(t) = (\dot{m}_{\beta,d}(t), u_{\phi,d})^\top$ ,  $u(t) = (\dot{m}_{\beta}(t), u_{\phi})^\top$ ,  $y(t) = (p_{mi}(t), \lambda(t))^\top$ .

Additionally, the frequency-dependent weights  $W_u(s)$  and  $W_p(s)$ , normalized to 1 at DC frequency, are introduced to specify the frequency range at which  $T_1(s)$  and  $S_O(s)$ , respectively, should be large. To achieve zero steady-state offset from the modeled disturbances up to a bandwidth close to the theoretical maximum of a pure delay system,  $\omega_{\max} = \frac{1}{T_{\max}}$ , proper weights of  $W_u(s) = \text{diag}\left(\frac{1000 \cdot s + 5000}{5 \cdot s + 5000}, \frac{1000 \cdot s + 5000}{5 \cdot s + 5000}\right)$  and  $W_p(s) = \text{diag}\left(\frac{s+2}{2 \cdot s+0.002}, \frac{s+5}{2 \cdot s+0.005}\right)$  are chosen. These weights result in a system with approximate bandwidths of 1 rad/s and 2.5 rad/s in  $y(t)$ , respectively. To maintain validity of the model formulation, the maximum controllable frequency is set at a conservative 5 rad/s.

The final feedback controller is then found through the use of the *hinfsyn* command available as part of the MATLAB robust control toolbox (Balas, Chiang, Packard, & Safonov, 2022).

#### 4. Cylinder individual reference tracking

For a cycle-based  $p_{mi}$  and  $\lambda$  reference tracking, the following actuating variables are necessary: the injection duration, the valve timings, and the ignition timing. The model described in Section 3 outputs the injection duration and the valve timings accordingly to the requested  $p_{mi}$ . The model is capable to consider variations in  $\lambda$ . However, the scope of this project is limited to  $\lambda = 1$ , i.e. to stoichiometric combustion. Furthermore, the EGR rate is included in the Willans fit of the model, although measurements have shown that its influence on  $p_{mi}$  and  $\lambda$  are marginal and thus can be neglected in the feedforward control. The ignition timing required for an optimal combustion with a center of 8 °CA after TDC is stored in a two-dimensional fit, which is dependent on the desired value of  $p_{mi}$  and the amount of EGR. The value stored in this fit is applied in a feedforward manner to the ignition coil. The center of combustion is computed in real-time for each firing event and used in a feedback control circuit to adapt the ignition timing such that the combustion is optimal.

##### 4.1. Reference tracking of $p_{mi}$ and $\lambda$

In this section, the performance of the reference tracking controller is presented and analyzed. Here, the EGR rate is kept at its minimal value, i.e.  $u_{IVO}$  and  $u_{EVC}$  remain at 0 °CA which is at TDC. The mean absolute errors of all experiments conducted are summarized in Table 2.

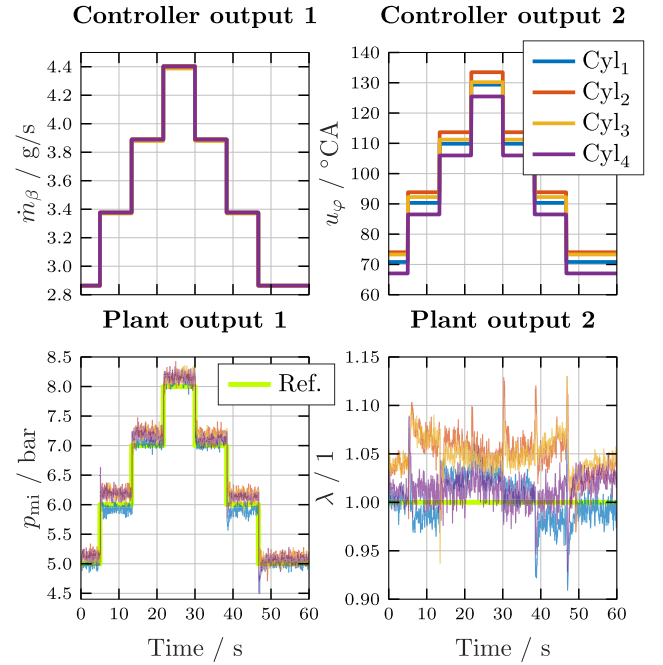


Fig. 6. Results of reference tracking obtained from the engine test bench the feedforward controller  $K_{ff}$  only and a full neural network. The upper plots show the outputs of the controller, i.e. the air mass flow  $\dot{m}_{\beta}$  and the injection duration  $u_{\phi}$ , for each cylinder. The lower plots show the  $p_{mi}$  and  $\lambda$  values for each cylinder over the reference trajectory, which contains steps in  $p_{mi}$  and is constant for  $\lambda$ .

**System behavior with feedforward only control.** In Fig. 6, the results from the reference tracking with the feedforward controller  $K_{ff}$  only and a full neural network are visualized over time. The upper left plot shows the controller output  $\dot{m}_{\beta}$  in g/s, which is the desired air mass flow for each cylinder. The value of  $\dot{m}_{\beta}$  required to achieve a certain  $p_{mi}$  is dependent on the air-to-fuel ratio, which is kept constant, and the Willans efficiency, which does not vary substantially between the individual cylinders. Thus, the differences in  $\dot{m}_{\beta}$  from Cylinders 1 to 4 are marginal and, thus, not clearly distinguishable in the plot. The upper right plots show the cylinder individual injection duration  $u_{\phi}$  in °CA. Between Cylinders 1 to 4, it varies for the same load by up to 6.4% from the overall mean value. This result indicates the significance of the parameter identification for every individual fuel injector.

The bottom plots present the outputs of the plant, i.e. the engine. In the left plot, the  $p_{mi}$  value of each combustion event and of each cylinder as well as the reference trajectory are shown. The load reference trajectory starts at a  $p_{mi}$  value of 5 bar, increases its value to a  $p_{mi}$  of 8 bar, and decreases it back to the initial value over a measurement duration of 60 seconds. The step size is kept at a constant value of 1 bar. On the right-hand side, the  $\lambda$  value measured in the exhaust runner of each cylinder is plotted as well as the constant reference value of 1. The air-to-fuel equivalence factor  $\lambda$  has a mean absolute error (MAE) of 0.033 averaged over all cylinders. The inner cylinders, Cylinder 2 and 3, are running at a very similar, rather lean value of  $\lambda$ . The outer cylinder group is running at almost stoichiometric values. The MAE in  $p_{mi}$  averaged over all cylinders is 0.14 bar. At lower  $p_{mi}$  values, an overshooting and subsequent convergence to a steady state is observed for the outer cylinder group. This is valid especially for load shedding, i.e. at the time stamps 38 s and 47 s, but also for load steps such as at time stamp 5 s. Such a behavior can be explained by the output of the neural network. At low loads, i.e. for values smaller than 7 bar, the volumetric efficiency of Cylinders 1 and 4 is significantly more affected by the value of  $p_{IM}$  than the one of the inner cylinder group. Thus, the prediction of  $u_{IVC}$  with a full neural network is highly sensitive to the value of  $p_{IM}$ . This behavior can be prevented by training the neural

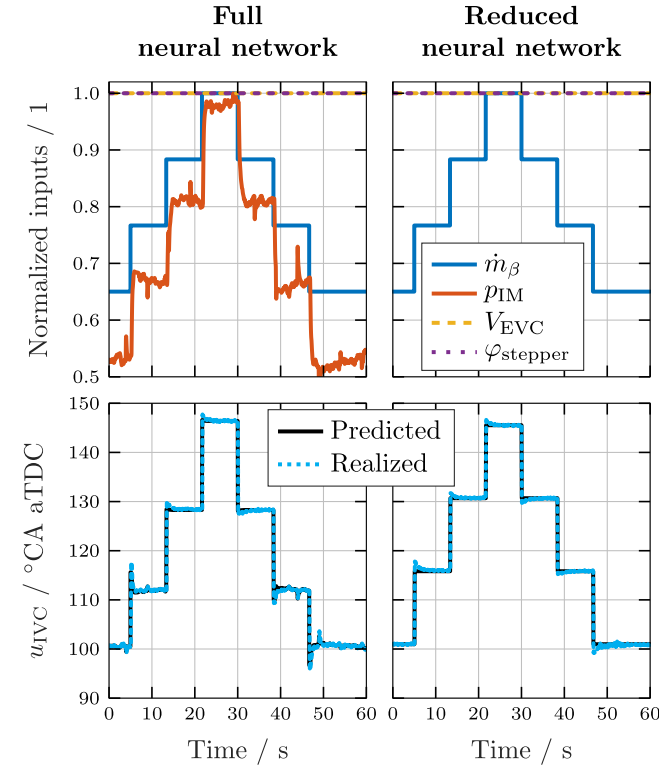


Fig. 7. Comparison of a full and a reduced neural network, i.e. a neural network with the intake manifold pressure  $p_{IM}$  as a feature included and one without it.

network without comprising  $p_{IM}$  as a feature, which leads to a reduced neural network, as it is called in this paper.

**Comparison of a full and a reduced neural network.** In this paper, the inputs of a full neural network are the cylinder specific air mass flow  $\dot{m}_\beta$ , the pressure in the intake manifold  $p_{IM}$ , the cylinder volume at the EVC instance  $V_{EVC}$ , and the stepper motor position  $\varphi_{stepper}$ . The engine is always operated with a wide open throttle, since the FlexWork FVVT allows to adjust the cylinder charge by Miller valve timings. Nevertheless, when comparing low load to full load operation, variations in the range of a few hundred pascals are observed in the  $p_{IM}$  signal. Experiments have shown that the volumetric efficiency is affected by these variations, which is particularly evident for the outer cylinder group. However, the input  $p_{IM}$  is a measured signal and thus underlies sensor noise and system dynamics, i.e. delays. By excluding  $p_{IM}$  from the feature set, a reduced neural network is trained. This increases the robustness of the prediction of  $u_{IVC}$  at the cost of accuracy. In this section, the  $p_{mi}$  and  $\lambda$  tracking performance is analyzed depending on the choice of the neural network. Fig. 7 visualizes the effect of a particular neural network on the  $u_{IVC}$  prediction. In the upper plots, the inputs normalized by their respective maxima are visualized while the predicted IVC valve timing and the IVC valve timing realized by the valve train are presented in the lower plots in °CA after TDC. The predicted  $u_{IVC}$  is the desired value sent to the low-level controller of the FVVT which is subsequently translated into a current duration and applied to the magnetic coils. The  $u_{IVC}$  realized is the measurement of the crank angle when the valve lift during the closing procedure equals a threshold of 0.25 mm. On the left-hand side, the results of the full neural network are shown, while on the right-hand side the results of the reduced neural network are shown. In this particular show case, only  $\dot{m}_\beta$  and  $p_{IM}$  are relevant since  $V_{EVC}$  and  $\varphi_{stepper}$  remain constant for both variants of the neural network. The main difference between the two is the  $u_{IVC}$  prediction visualized by the black solid lines. For low-load operating points, i.e. for  $u_{IVC} < 120$  °CA after TDC,

Table 2

Mean absolute errors in  $p_{mi}$  and  $\lambda$  for all cylinders when tracking a given trajectory either with a feedforward (FF) controller only or with an additional feedback (FB) controller. Additionally, the different errors measured by applying either a full neural network (NN<sub>full</sub>) or a reduced neural network (NN<sub>red</sub>) are stated. Values marked with (̄) are averaged over all cylinders.

	FF NN <sub>full</sub>	FF NN <sub>red</sub>	FB NN <sub>full</sub>	FB NN <sub>red</sub>
$p_{mi,1}$	0.09 bar	0.16 bar	0.08 bar	0.07 bar
$p_{mi,2}$	0.19 bar	0.16 bar	0.08 bar	0.07 bar
$p_{mi,3}$	0.15 bar	0.21 bar	0.07 bar	0.07 bar
$p_{mi,4}$	0.14 bar	0.20 bar	0.07 bar	0.07 bar
$\bar{p}_{mi}$	<b>0.14 bar</b>	<b>0.18 bar</b>	<b>0.07 bar</b>	<b>0.07 bar</b>
$\lambda_1$	0.019	0.025	0.010	0.009
$\lambda_2$	0.050	0.054	0.011	0.009
$\lambda_3$	0.049	0.068	0.008	0.009
$\lambda_4$	0.016	0.025	0.010	0.011
$\bar{\lambda}$	<b>0.033</b>	<b>0.043</b>	<b>0.010</b>	<b>0.009</b>

the prediction of the full neural network is affected by the  $p_{IM}$  signal. At load transitions, where  $p_{IM}$  is delayed due to the physical properties of the intake manifold, the neural network attempts to compensate for this effect by predicting  $u_{IVC}$  accordingly. Since it is trained only on steady-state measurement data, this compensation is actually an overcompensation which eventually leads to an overshooting in  $p_{mi}$  and  $\lambda$  as shown in Fig. 6. In contrast, the prediction of the reduced neural network relies only on the controller output  $\dot{m}_\beta$  and thus exhibits a very robust behavior.

Regardless of the choice of the neural network, the  $u_{IVC}$  realized follows the predicted  $u_{IVC}$  well for small steps. However, at larger steps such as at the time stamps 5 s, 13 s, or 22 s, a mismatch occurs stemming from the electrical part of the valve train. A desired valve timing is converted with a feedforward map to a timing of the electric current. The valve lift realized is measured, followed by a feedback controller adjusting the electric current timing such that the desired valve timing is achieved. However, the effect of the inaccuracy between predicted and realized IVC is negligible.

As summarized in Table 2, in a pure feedforward control setting a full neural network performs approximately 29% better than a reduced neural network. Despite the unsteady  $u_{IVC}$  prediction, the volumetric efficiency is estimated closer to its true value if  $p_{IM}$  is known, causing the improvement in  $p_{mi}$  and  $\lambda$ . However, if  $K_{ff}$  is extended by  $K_{fb}$ , the performance of the two neural networks are almost identical. In fact, the reduced neural network performs marginally better than the full one since the feedback controller handles a static offset better than a dynamic one.

The simultaneous steps in  $u_{IVO}$  and  $u_{EVC}$  cause significant peaks in the  $p_{IM}$  signal, which leads to a wrong prediction of  $u_{IVC}$ . Thus, during the EGR rate optimization presented in the following section, a reduced neural network is used for the  $u_{IVC}$  prediction.

**System behavior with feedforward and feedback control.** Fig. 8 shows the results obtained when in addition to the feedforward controller  $K_{ff}$ ,  $K_{fb}$  is an  $H_\infty$  controller, as presented in Fig. 4. The reference trajectories here are identical to those presented in Fig. 6. However, for a clearer visualization, only the data obtained from one cylinder is plotted Fig. 8. Additionally, for a detailed view, only the time window from 37 s to 50 s, i.e. the two load steps from 7 bar to 5 bar, are shown. However, the observations made here are valid for all cylinders and the complete reference trajectory.

The upper left plot shows the inputs to the reduced neural network, which are the cylinder specific air mass flow  $\dot{m}_\beta$ , the cylinder volume at the EVC instance  $V_{EVC}$ , and the stepper motor position  $\varphi_{stepper}$ . All inputs to the neural network are normalized with respect to their respective maxima. Here, as in the scenario of the pure feedforward control shown in Fig. 6,  $V_{EVC}$  and  $\varphi_{stepper}$  remain constant. The upper middle plot shows the controller output  $\dot{m}_\beta$ . The gray dashed line is



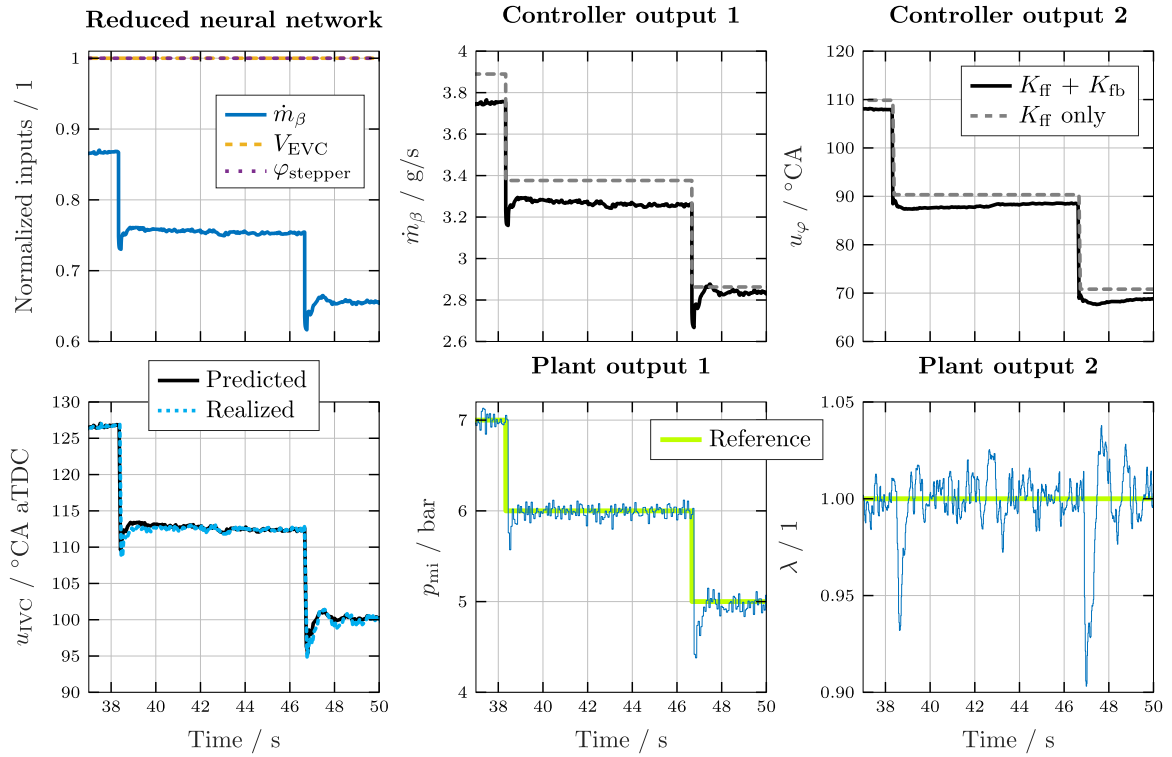


**Fig. 8.** Results of  $p_{mi}$  and  $\lambda$  reference tracking obtained with a combination of a feedforward controller  $K_{ff}$ , an  $H_\infty$  feedback controller  $K_{fb}$ , and a reduced neural network. For a detailed analysis, only the data obtained from one cylinder and during a restricted time frame is plotted.

the output from the  $K_{ff}$  controller and the black solid line represents the sum of the  $K_{ff}$  and  $K_{fb}$  controllers. The same holds true for the upper right plot, which shows the injection duration  $u_\phi$ . The plot on the bottom left shows the value of  $u_{IVC}$  predicted by the neural network and realized by the FVVT in °CA after TDC. The  $p_{mi}$  value of each combustion event of one cylinder as well as the reference trajectory are plotted in the middle bottom plot. In the right bottom plot, the  $\lambda$  value measured in one exhaust runner is plotted as well as the constant reference value of 1.

The MAE of the  $p_{mi}$  averaged over all cylinders is equal to 0.07 bar, while the MAE of the  $\lambda$  value equals 0.009. For both outputs  $p_{mi}$  and  $\lambda$ , all cylinders exhibit a similar performance. Compared to the tracking performance with pure feedforward control and a reduced neural network, an improvement of 62% in  $p_{mi}$ , and of 79% in  $\lambda$  is achieved with feedback control.

The output of Controller 1 clearly shows that towards higher loads the mismatch between the feedforward and the feedback output is larger than towards lower loads. This mismatch can be explained by the linearization point of  $\dot{m}_\beta$ , which is set to 2 g/s. The reason for this rather low value is twofold. On the one hand, at low loads the Willans efficiency shown in (11) has a steep gradient. On the other hand, at values of  $u_{IVC}$  around 90 °CA after TDC, the piston speed and therefore the air flow over the intake valves is maximal. Thus, at low loads, small errors in the estimation of the required air flow, either due to the Willans approximation or due to the  $u_{IVC}$  prediction, lead to high discrepancies in the target  $p_{mi}$  value. These discrepancies can be minimized when the plant model is linearized at a low-load operating point, such that it fits the nonlinear model. At high loads, both the Willans approximation and the  $u_{IVC}$  prediction are less sensitive to the change in the corresponding inputs, and thus, the model is more robust.

Comparing Output 1 and Output 2 of the controller, a much more aggressive strategy for  $\dot{m}_\beta$  can be observed. This is due to the parametrization of the  $H_\infty$  controller. In this scenario, an accurate tracking of the target  $p_{mi}$  value is chosen over the tracking of the  $\lambda$  value. Output 1 of the plant shows that after a load step the target value of  $p_{mi}$  is

achieved in a few cycles. The overshoot at the instance of the load step is not present when using the feedforward controller  $K_{ff}$  only in combination with a reduced neural network. Thus, at the cost of a slower convergence to the target value, the feedback controller  $K_{fb}$  can be parameterized to minimize overshooting. Since Output 2 of the controller, the injection duration  $u_\phi$ , is set to be much less aggressive, peaks in the value of  $\lambda$  during load steps are unavoidable when  $\dot{m}_\beta$  is over- or underestimated. Since both the air flow rate and the injection duration are affecting the  $p_{mi}$  and  $\lambda$  value, strong cross-coupling effects are present. Thus, it is not feasible to set both controller to an equal sensitivity. However, if necessary, the  $\lambda$  tracking can be favored over the  $p_{mi}$  tracking in the controller design.

Finally, with the reduced neural network the prediction of  $u_{IVC}$  solely depends on the controller Output 1, i.e. on  $\dot{m}_\beta$ . The aggressive changes in  $\dot{m}_\beta$  are well converted in a fast changing  $u_{IVC}$  and is well tracked by the FVVT. Only if a full neural network is used, the noisy  $p_{IM}$  signal adds an additional disturbance to the tracking objective, which leads to a slightly worse overall performance.

#### 4.2. Reference tracking with online optimization of the EGR rate

Among other things, using an EGR can help to reduce the emission of pollutants such as  $NO_x$ . As described in Section 3, with this test bench setup the amount of residual gas is minimized when  $u_{IVO/EVC} = 0$  °CA, i.e. at TDC. To increase the amount of residual gas,  $u_{IVO/EVC}$  is delayed such that it occurs after TDC. An external re-induction over the intake manifold is not required. Thus, with an FVVT the rate of EGR can be set arbitrarily by choosing  $u_{IVO/EVC}$  accordingly, which is much faster than the adjustments of an external EGR path leading over the intake manifold. Fig. 9 shows an overview of the emission measurement data obtained from steady-state operation. On the left-hand side, emission concentrations in ppm are visualized over the measured range of  $p_{mi}$  and over  $u_{IVO/EVC}$ . The concentration of  $NO_x$  pollutants is plotted in the upper left corner, while the concentration of HC pollutants is plotted in the lower left corner. Each triangle represents a steady-state measurement and the two planes show the corresponding fit.

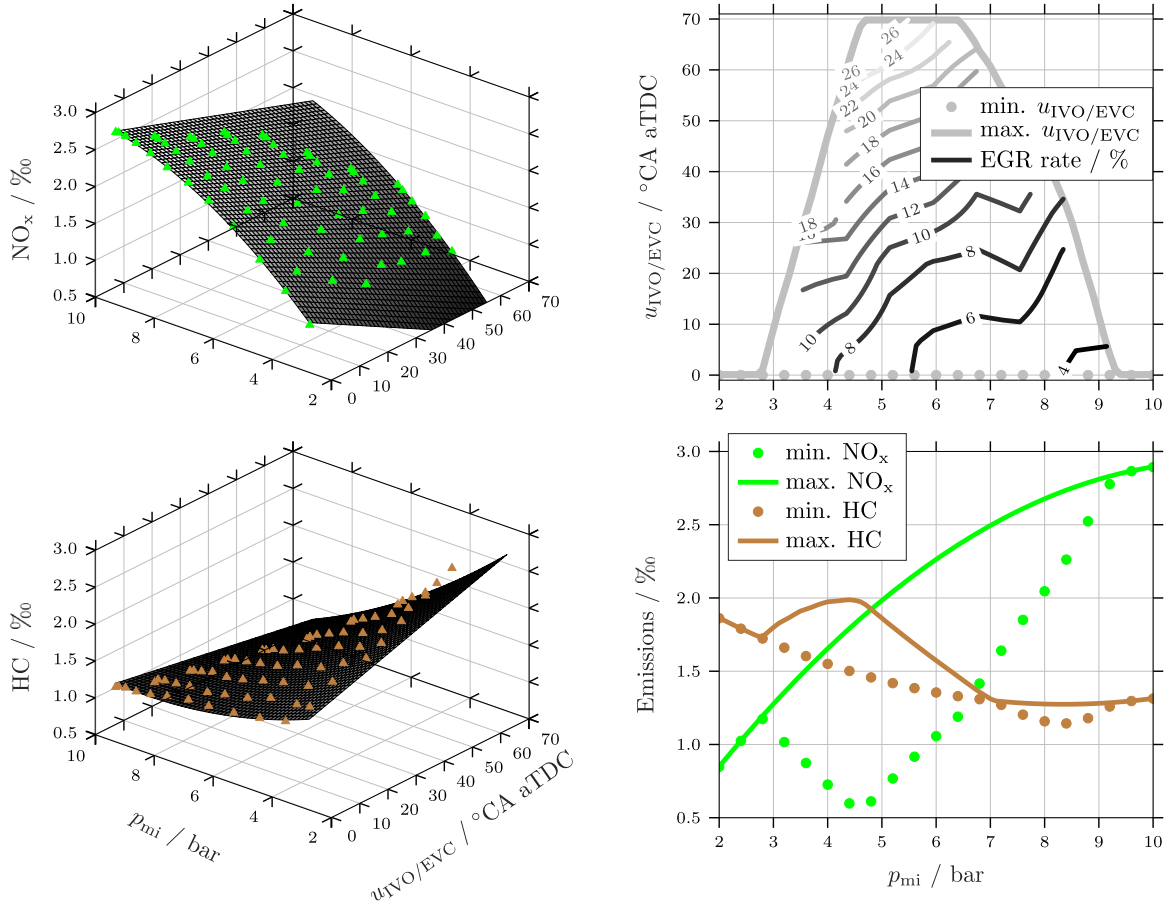


Fig. 9. Emission data obtained from steady-state operation. On the left-hand side, the measurement points are indicated with triangles and the accordingly fitted models as planes. The upper right plot shows the boundaries for  $u_{IVO/EVC}$  and the achieved EGR rate in percent. The bottom right plot shows the achievable minimal and maximal pollutant emission concentrations in regard to the  $u_{IVO/EVC}$  boundaries. (For interpretation of the references to color in this figure legend, the reader is referred to the web version of this article.)

For both pollutants, the fit is obtained with a quadratic relation to  $p_{mi}$  and a linear relation to  $u_{IVO/EVC}$ . The  $R^2$  value for the  $\text{NO}_x$  fit is 0.997 with a root mean squared error of 35 ppm. In case of the HC fit, the  $R^2$  value is 0.956 with a root mean squared error of 49 ppm. In the upper right corner, the boundaries of  $u_{IVO/EVC}$  and the estimated EGR rate in percent are plotted over  $p_{mi}$ . The minimal  $u_{IVO/EVC}$ , plotted as dots, leads to a minimal EGR rate and always lies at TDC. The maximal  $u_{IVO/EVC}$ , plotted as a solid line, is determined by the maximally possible EGR rate for a certain cylinder load. Below a  $p_{mi}$  of 4.6 bar,  $u_{IVO/EVC}$  must be decreased linearly to the load. Otherwise the combustion duration becomes too long and a center of combustion of 8°CA cannot be maintained. Above a  $p_{mi}$  of 6.4 bar,  $u_{IVO/EVC}$  must be decreased proportionally to the increase of the load such that enough fresh mixture can be inducted into the cylinder to achieve the desired load. Between  $p_{mi}$  values of 4.6 bar and 6.4 bar, 70°CA after TDC is the maximal  $u_{IVO/EVC}$  instance, because a further increase would lead to an unstable combustion since the mixture would not ignite reliably. In the lower right corner, the concentration extrema of the pollutants, which are bounded by the achievable EGR rates depending on the load, are plotted over  $p_{mi}$ . The maximal  $\text{NO}_x$  concentration, plotted as a solid green line, increases monotonically over the  $p_{mi}$  range. The minimal  $\text{NO}_x$  concentration is plotted as dots. From a  $p_{mi}$  value of 2.8 bar to 4.6 bar, the minimal  $\text{NO}_x$  concentration decreases monotonically to a global minimum of 557 ppm. Up to a  $p_{mi}$  of 6.4 bar, the minimal  $\text{NO}_x$  concentration increases linearly with the load since  $u_{IVO/EVC}$  remains constant. Above a  $p_{mi}$  of 6.4 bar, the increase rate rises since a further increase in load requires a decrease in the EGR rate. At the low and at the high end of the  $p_{mi}$  range, the minimal and maximal  $u_{IVO/EVC}$  values are identical. The minimal and maximal concentrations of both pollutants, respectively, thus coincide there.

The HC concentration is plotted in brown, with a solid line for the maximal values and with dots for the minimal values. In contrast to the  $\text{NO}_x$  emissions, the HC exhibits a switching behavior with regard to the EGR rate. Below a  $p_{mi}$  value of 7 bar, an increase in the EGR rate leads to an increase of HC emissions. Above a  $p_{mi}$  value of 7 bar, the tendency is inverted and an increased EGR rate leads to a reduction of HC emissions. This is explained as follows: At a high load, the compression ratio and thus the charge density increases and there is more turbulence than at a low load. This also increases the pre-combustion temperature level, which ultimately leads to an increase in exhaust gas temperature. As a result, HC molecules are more likely to be oxidized when the exhaust gases are recirculated at high engine loads. On the other hand, increasing the EGR rate at a low load dilutes the charge, which slows down the combustion process and causes more HC emissions due to incomplete combustion.

The highest difference between the minimum and the maximum for both pollutants lies at a  $p_{mi}$  value of 4.6 bar and amounts to 70% for the  $\text{NO}_x$  concentration and to 25% for the HC concentration.

In order to prioritize the minimization of either  $\text{NO}_x$  or HC pollutants, a cost function with a weighting factor is required, as defined by

$$J_{\text{NO}_x} = \alpha \cdot (C_{\text{NO}_x})^2, \quad (12)$$

$$J_{\text{HC}} = (1 - \alpha) \cdot (C_{\text{HC}})^2, \quad (13)$$

$$J_{\text{tot}} = J_{\text{NO}_x} + J_{\text{HC}}. \quad (14)$$

The variable  $J_{\text{tot}}$  represents the sum of the pollutant-specific cost functions  $J_{\text{NO}_x}$  and  $J_{\text{HC}}$  and is subject to optimization, while  $C_{\text{NO}_x}$  and  $C_{\text{HC}}$  are the pollutant-specific concentrations and  $\alpha$  is the weighting

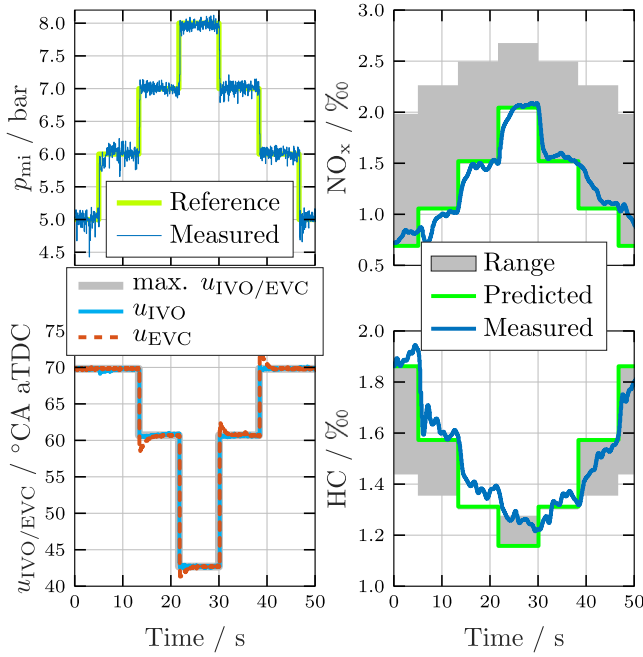


Fig. 10. Results of the  $p_{mi}$  and  $\lambda$  reference tracking with an online optimization of the internal exhaust gas recirculation rate. These results are achieved with the cost function parameter  $\alpha$  set to 1. (For interpretation of the references to color in this figure legend, the reader is referred to the web version of this article.)

factor. Fig. 10 shows the results of an online  $u_{IVO/EVC}$  optimization during the reference tracking of  $p_{mi}$  and  $\lambda$  for a fixed  $\alpha$  value of 1. The upper left plot shows the  $p_{mi}$  values of a single cylinder and the reference trajectory. The mean absolute error in  $p_{mi}$  equals 0.08 bar and in  $\lambda$  a value of 0.008. These values are in the same range as the MAE for the trajectory tracking with a constant  $u_{IVO/EVC}$ , as listed in Table 2. This results confirms the prediction that the input responsible for the EGR rate is rather well decoupled from the inputs responsible for the load and the stoichiometry of the combustion. The bottom left plot shows the realized values of  $u_{IVO}$  and  $u_{EVC}$  as well as the load-dependent maximally possible values of  $u_{IVO/EVC}$ . Since for this scenario  $\alpha = 1$ , the EGR rate is maximized for every operating point in order to minimize the  $NO_x$  emissions without regard to the HC emissions. Thus,  $u_{IVO}$  and  $u_{EVC}$  coincide with the maximally possible value of  $u_{IVO/EVC}$  for the complete trajectory duration. Conspicuously, the  $u_{IVO}$  follows the desired steps accurately, while  $u_{EVC}$  overshoots at every step. This is explained by the current duration applied on the magnetic coils of the FVVT system. Delaying  $u_{IVO}$  tends to shorten the duration during which the intake valves are open, i.e. the current duration applied on the magnetic coils. In contrast, delaying  $u_{EVC}$  prolongs the current duration applied on the magnetic coils of the exhaust valves. The longer the current duration applied on these coils is, the more significant are the electrical effects such as magnetic hysteresis. Thus, the feedforward controller for  $u_{EVC}$  is more prone to errors than for  $u_{IVO}$ . The right-hand side of these plots shows the results of pollutant concentrations. The gray areas represent the possible range between minimal and maximal pollutant concentrations that can be achieved with the appropriate  $u_{IVO/EVC}$  setting. The green lines show the predicted pollutant concentrations, which are the results of the minimization of (14) with the given  $\alpha$ . The blue lines are the actual measurement of the corresponding pollutants. As expected due to the choice of  $\alpha = 1$ , the prediction of the  $NO_x$  concentration lies at the bottom end of the gray area. Although the edges are less distinguished, the measurement fits the prediction well. This is true for the concentrations of  $NO_x$  as well as for HC. In the lower right plot the switching behavior in the HC concentration is well illustrated. From 0 s to 13 s and from 38 s to 60 s the reference

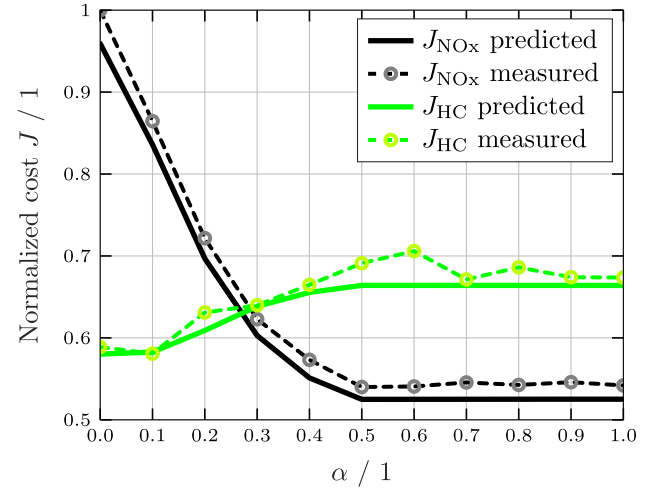


Fig. 11. Comparison of the prediction and the measurement of the cost  $J_{NO_x}$  and  $J_{HC}$  when varying the weighting factor  $\alpha$ . Each data point is the result of averaging the particular cost values over the complete duration of the trajectory tracking during which the  $\alpha$  value is kept constant.

$p_{mi}$  is clearly below 7 bar. A maximal  $u_{IVO/EVC}$  value thus leads to a maximal HC concentration. From 13 s to 22 s and from 30 s to 38 s the reference  $p_{mi}$  is at 7 bar, which marks the switching point of the trend in HC concentration. Thus, in this region, basically no optimization is possible, i.e. any value of  $u_{IVO/EVC}$  leads to the same HC concentration. Finally, from 22 s to 30 s the reference  $p_{mi}$  is above 7 bar. Hence, a maximal  $u_{IVO/EVC}$  value leads to a minimal HC concentration.

Fig. 11 shows the influence of the cost function parameter  $\alpha$  on the cost  $J$  for both pollutants. For each  $\alpha$  value, the optimization of  $u_{IVO/EVC}$  is conducted on the trajectory shown in Fig. 10. The values of  $J_{NO_x}$  and  $J_{HC}$  then are averaged over the trajectory and normalized with respect to the global maximum. The solid lines represent the cost prediction based on the emission fits. The dashed lines represent the cost obtained from measurement data. The mean relative error between fit and measurement equals 3.6% for the  $NO_x$  cost and 2.3% for the HC cost. As (14) shows, for low  $\alpha$  values the minimization of HC pollutants is favored over  $NO_x$  pollutants and vice versa for high  $\alpha$  values. Over the range from  $\alpha = 0$  to  $\alpha = 0.5$ , the average  $NO_x$  cost is reduced by 46%. Meanwhile, the average HC cost is increased by 17%. For the given trajectory and cost function  $J_{tot}$ , a further increase of the  $\alpha$  value above 0.5 does not lead to any further changes in the specific cost values.

## 5. Conclusion and outlook

In this paper we investigated the possibilities of a cylinder-individual load and air-to-fuel equivalence factor  $\lambda$  reference tracking enabled by a fully variable valve train, which is able to adapt the intake and exhaust valve timings on a cycle-to-cycle basis. A mean-value model is used to mathematically describe the processes inside an internal combustion engine such as injection, exhaust gas recirculation, and torque generation. The influence of the valve timings on the air flow through the engine is treated in separation. A neural network is trained to map the volumetric efficiency in order to predict the intake valve closing instance corresponding to the desired cylinder charge. The inversion of this neural network leads to cancellation of non-linearity which simplifies the application of common linearization methods. All models are fitted with data obtained from measurements on an engine test bench. The experiments are conducted on a 1.4 L spark-ignited engine which is equipped with an internally developed fully variable valve train called FlexWork. The main findings of this study can be summarized as follows:

- Based on a mean-value model, a feedback controller is constructed with a mixed-sensitivity  $H_\infty$  synthesis method.
- A single multi-layer perceptron regressor with a single hidden layer and a rectified linear unit activation function estimates the required intake valve closing instance for a specific air mass flow with an  $R^2$  score of 0.99.
- The model-based feedforward controller achieves a mean absolute error of 0.14 bar in the mean indicated pressure and of 0.033 in  $\lambda$  for the given trajectory. With a feedback controller based on a  $H_\infty$  synthesis method a mean absolute error of 0.07 bar in the mean indicated pressure and of 0.009 in  $\lambda$  is achieved for the given trajectory.
- The internal exhaust gas recirculation rate is adapted online depending on an emission cost function without significantly affecting the tracking performance.
- By adjusting the weighting parameter of the emission cost function, either the  $\text{NO}_x$  emissions are reduced by up to 46% or the HC emissions by up to 17% over the range of the trajectory. The mean relative error between pollutant fit and measurement equals 3.6% for the  $\text{NO}_x$  cost and 2.3% for the HC cost.

**Outlook.** In the current model, the stoichiometry sensors are modeled with a time delay only. To further improve the tracking performance, an advanced sensor model or state estimator would be desirable. The scope of this paper was to investigate a stoichiometric combustion only. Any extension to non-stoichiometric applications, as e.g. for the aftertreatment system beneficial rich/lean oscillations, would require an extension of the measurement grid. While a reduced neural network proved to be useful due to its robustness, a full neural network might be required for applications with the use of a throttle, as e.g. the control of external EGR. In addition to load and emission trajectory tracking, such an FVVT system can be used to improve the heat-up process of exhaust gas aftertreatment systems. One approach that requires further investigation is early exhaust valve opening to allow for increased enthalpy flow to the exhaust while maintaining an optimal center of combustion.

## Declaration of competing interest

The authors declare that they have no known competing financial interests or personal relationships that could have appeared to influence the work reported in this paper.

## References

- Akansu, S., Dulger, Z., Kahraman, N., & Veziroglu, T. (2004). Internal combustion engines fueled by natural gas-hydrogen mixtures. *International Journal of Hydrocarbon Engineering*, 29(14), 1527–1539. <http://dx.doi.org/10.1016/j.ijhydene.2004.01.018>.
- Alshammari, M., Alshammari, F., & Pesyridis, A. (2019). Electric boosting and energy recovery systems for engine downsizing. *Energies*, 12(24), 4636. <http://dx.doi.org/10.3390/en12244636>.
- Alvarez, C. E. C., Couto, G. E., Roso, V. R., Thiriet, A. B., & Valle, R. M. (2018). A review of prechamber ignition systems as lean combustion technology for SI engines. *Applied Thermal Engineering*, 128, 107–120. <http://dx.doi.org/10.1016/j.applthermaleng.2017.08.118>.
- Awad, O. I., Ma, X., Kamil, M., Ali, O. M., Ma, Y., & Shuai, S. (2020). Overview of polyoxymethylene dimethyl ether additive as an eco-friendly fuel for an internal combustion engine: Current application and environmental impacts. *Science of the Total Environment*, 715, Article 136849. <http://dx.doi.org/10.1016/j.scitotenv.2020.136849>.
- Awogbemi, O., Kallon, D. V. V., Onuh, E. I., & Aigbodion, V. S. (2021). An overview of the classification, production and utilization of biofuels for internal combustion engine applications. *Energies*, 14(18), 5687. <http://dx.doi.org/10.3390/en14185687>.
- Balas, G., Chiang, R., Packard, A., & Safonov, M. (2022). *Robust control toolbox user's guide*.
- Balmelli, M., Zsiga, N., Merotto, L., & Soltic, P. (2020). Effect of the intake valve lift and closing angle on part load efficiency of a spark ignition engine. *Energies*, 13(7), 1682. <http://dx.doi.org/10.3390/en13071682>.
- Benajes, J., García, A., Monsalve-Serrano, J., & Martínez-Boggio, S. (2019). Optimization of the parallel and mild hybrid vehicle platforms operating under conventional and advanced combustion modes. *Energy Conversion and Management*, 190, 73–90. <http://dx.doi.org/10.1016/j.enconman.2019.04.010>.
- Bozza, F., Bellis, V. D., & Teodosio, L. (2016). Potentials of cooled EGR and water injection for knock resistance and fuel consumption improvements of gasoline engines. *Applied Energy*, 169, 112–125. <http://dx.doi.org/10.1016/j.apenergy.2016.01.129>.
- Cammalleri, M., Pipitone, E., Beccari, S., & Genchi, G. (2013). A mathematical model for the prediction of the injected mass diagram of a S.I. engine gas injector. *Journal of Mechanical Science and Technology*, 27(11), 3253–3265. <http://dx.doi.org/10.1007/s12206-013-0848-6>.
- Caputo, S., Millo, F., Boccardo, G., Piano, A., Cifali, G., & Pesce, F. C. (2019). Numerical and experimental investigation of a piston thermal barrier coating for an automotive Diesel engine application. *Applied Thermal Engineering*, 162, Article 114233. <http://dx.doi.org/10.1016/j.applthermaleng.2019.114233>.
- Cardoso, J. S., Silva, V., Rocha, R. C., Hall, M. J., Costa, M., & Eusébio, D. (2021). Ammonia as an energy vector: Current and future prospects for low-carbon fuel applications in internal combustion engines. *Journal of Cleaner Production*, 296, Article 126562. <http://dx.doi.org/10.1016/j.jclepro.2021.126562>.
- Distaso, E., Amirante, R., Cassone, E., Palma, P. D., Sementa, P., Tamburrano, P., et al. (2020). Analysis of the combustion process in a lean-burning turbulent jet ignition engine fueled with methane. *Energy Conversion and Management*, 223, Article 113257. <http://dx.doi.org/10.1016/j.enconman.2020.113257>.
- Dolan, R. H., Anderson, J. E., & Wallington, T. J. (2021). Outlook for ammonia as a sustainable transportation fuel. *Sustainable Energy Fuels*, 5(19), 4830–4841. <http://dx.doi.org/10.1039/d1se00979f>.
- Dvadenko, V., Arhun, S., Bogajevskiy, A., & Ponikarovska, S. (2018). Improvement of economic and ecological characteristics of a car with a Start-Stop system. *International Journal of Electric and Hybrid Vehicles*, 10(3), 209. <http://dx.doi.org/10.1504/ijehv.2018.097377>.
- Emran, A., Ehrly, M., Sandhu, R., Chavan, S., SK, R., & Sharma, V. (2019). Approach towards engine downsizing with 48 Volt Diesel hybrid SUV meeting future emission legislations in India. In *2019 IEEE transportation electrification conference. IEEE*, <http://dx.doi.org/10.1109/itec-india48457.2019.itecindia2019-34>.
- Feng, D., Wei, H., & Pan, M. (2018). Comparative study on combined effects of cooled EGR with intake boosting and variable compression ratios on combustion and emissions improvement in a SI engine. *Applied Thermal Engineering*, 131, 192–200. <http://dx.doi.org/10.1016/j.applthermaleng.2017.11.110>.
- Fernandes, H., Pimenta, C. Q., Rodrigues, W. N., de Souza Montemor, R. B., & Barros, J. E. M. (2016). Experimental investigation of internal exhaust gas recirculation on a variable valve actuation spark ignition engine operating with gasoline and ethanol. In *SAE technical paper series*. SAE International, <http://dx.doi.org/10.4271/2016-36-0399>.
- Flierl, R., Lauer, F., Breuer, M., & Hannibal, W. (2012). Cylinder deactivation with mechanically fully variable valve train. *SAE International Journal of Engines*, 5(2), 207–215. <http://dx.doi.org/10.4271/2012-01-0160>.
- Fuinhas, J. A., Koengkan, M., Leitão, N. C., Nwani, C., Uzuner, G., Dehdar, F., et al. (2021). Effect of battery electric vehicles on greenhouse gas emissions in 29 European Union countries. *Sustainability*, 13(24), 13611. <http://dx.doi.org/10.3390/su132413611>.
- García, A., Monsalve-Serrano, J., Martínez-Boggio, S., & Wittek, K. (2020). Potential of hybrid powertrains in a variable compression ratio downsized turbocharged VVA Spark Ignition engine. *Energy*, 195, Article 117039. <http://dx.doi.org/10.1016/j.energy.2020.117039>.
- Gosala, D. B., Raghukumar, H., Allen, C. M., Shaver, G. M., McCarthy, J. E., & Lutz, T. P. (2021). Model-based design of dynamic firing patterns for supervisory control of diesel engine vibration. *Control Engineering Practice*, 107, Article 104681. <http://dx.doi.org/10.1016/j.conengprac.2020.104681>.
- Guzzella, L., & Onder, C. (2004). *Introduction to modeling and control of internal combustion engine systems* (1st ed.). ETH Zürich, Switzerland: Springer Berlin, Heidelberg.
- Guzzella, L., & Sciarretta, A. (2013). *Vehicle propulsion systems*. Berlin Heidelberg: Springer, <http://dx.doi.org/10.1007/978-3-642-35913-2>, URL.
- Haas, M., & Rauch, M. (2010). Electro-hydraulic fully variable valve train system. *ATZautotechnology*, 10(2), 38–43. <http://dx.doi.org/10.1007/bf03247163>.
- Hänggi, S., Frey, J., van Dooren, S., Diehl, M., & Onder, C. H. (2022). A modular approach for Diesel engine air path control based on nonlinear MPC. *IEEE Transactions on Control Systems Technology*, 1–16. <http://dx.doi.org/10.1109/tcst.2022.3228203>.
- Hoef, F. (2021). Internal combustion engine to electric vehicle retrofitting: Potential customers' needs, public perception and business model implications. *Transportation Research Interdisciplinary Perspectives*, 9, Article 100330. <http://dx.doi.org/10.1016/j.trip.2021.100330>.
- Hoppe, F., Thewes, M., Baumgarten, H., & Dohmen, J. (2015). Water injection for gasoline engines: Potentials, challenges, and solutions. *International Journal of Engine Research*, 17(1), 86–96. <http://dx.doi.org/10.1177/1468087415599867>.
- Horvath, S., Fasihi, M., & Breyer, C. (2018). Techno-economic analysis of a decarbonized shipping sector: Technology suggestions for a fleet in 2030 and 2040. *Energy Conversion and Management*, 164, 230–241. <http://dx.doi.org/10.1016/j.enconman.2018.02.098>.



- IEA (2022). Electric cars fend off supply challenges to more than double global sales, IEA, Paris. <https://www.iea.org/commentaries/electric-cars-fend-off-supply-challenges-to-more-than-double-global-sales>. (Accessed 29 November 2022).
- Judith, J., Neher, D., Kettner, M., Schwarz, D., & Klaisle, M. (2020). High efficiency by Miller valve timing and stoichiometric combustion for a naturally aspirated single cylinder gas engine. *SAE International Journal of Advances and Current Practices in Mobility*, 2(2), 1041–1057.
- Kalghatgi, G. (2018). Is it really the end of internal combustion engines and petroleum in transport? *Applied Energy*, 225, 965–974. <http://dx.doi.org/10.1016/j.apenergy.2018.05.076>.
- Koli, R., Egan, D., Zhu, Q., & Prucka, R. (2023). Nonlinear model predictive control of a DISI turbocharged engine with virtual engine co-simulation and real-time experimental validation. *Proceedings of the Institution of Mechanical Engineers, Part D (Journal of Automobile Engineering)*, Article 095440702211465. <http://dx.doi.org/10.1177/09544070221146586>.
- Kuruppu, C., Pesiridu, A., & Rajoo, S. (2014). Investigation of cylinder deactivation and variable valve actuation on gasoline engine performance. In *SAE technical paper series*. SAE International, <http://dx.doi.org/10.4271/2014-01-1170>.
- Leone, T. G., & Pozar, M. (2001). Fuel economy benefit of cylinder deactivation - sensitivity to vehicle application and operating constraints. In *SAE technical paper series*. SAE International, <http://dx.doi.org/10.4271/2001-01-3591>.
- Lou, Z., & Zhu, G. (2020). Review of advancement in variable valve actuation of internal combustion engines. *Applied Sciences*, 10(4), 1216. <http://dx.doi.org/10.3390/app10041216>.
- Maas, G., Neukirchner, H., Dingel, O., & Predelli, O. (2004). Potential of an innovative, fully variable valvetrain. In *SAE technical paper series*. SAE International, <http://dx.doi.org/10.4271/2004-01-1393>.
- Mafrić, S. (2020). Study of friction reduction potential in light-duty Diesel engines by lightweight crankshaft design coupled with low viscosity oil. In *SAE technical paper series*. SAE International, <http://dx.doi.org/10.4271/2020-37-0006>.
- Malaquias, A. C. T., Netto, N. A. D., Filho, F. A. R., da Costa, R. B. R., Langeani, M., & Baêta, J. G. C. (2019). The misleading total replacement of internal combustion engines by electric motors and a study of the Brazilian ethanol importance for the sustainable future of mobility: a review. *Journal of the Brazilian Society of Mechanical Sciences and Engineering*, 41(12), <http://dx.doi.org/10.1007/s40430-019-2076-1>.
- Mathworks (2022). *Simulink control design user's guide*.
- Muratori, M., Alexander, M., Arent, D., Bazilian, M., Cazzola, P., Dede, E. M., et al. (2021). The rise of electric vehicles—2020 status and future expectations. *Progress in Energy*, 3(2), Article 022002. <http://dx.doi.org/10.1088/2516-1083/abe0ad>.
- Oh, S., Cho, S., Seol, E., Song, C., Shin, W., Min, K., et al. (2018). An experimental study on the effect of Stroke-to-Bore ratio of Atkinson DISI engines with variable valve timing. *SAE International Journal of Engines*, 11(6), 1183–1193. <http://dx.doi.org/10.4271/2018-01-1419>.
- Omanovic, A., Zsiga, N., Soltic, P., & Onder, C. (2021). Increased internal combustion engine efficiency with optimized valve timings in extended stroke operation. *Energies*, 14(10), 2750. <http://dx.doi.org/10.3390/en14102750>.
- Onofrio, G., Napolitano, P., Abagnale, C., Guido, C., & Beatrice, C. (2021). Model development of a CNG active pre-chamber fuel injection system. In *SAE technical paper series*. SAE International, <http://dx.doi.org/10.4271/2021-24-0090>.
- Pélerin, D., Gaukel, K., Härtl, M., Jacob, E., & Wachtmeister, G. (2020). Potentials to simplify the engine system using the alternative Diesel fuels oxymethylene ether OME1 and OME3-6 on a heavy-duty engine. *Fuel*, 259, Article 116231. <http://dx.doi.org/10.1016/j.fuel.2019.116231>.
- Pischinger, S. (2019). Synthetic fuels. *MTZ Worldwide*, 80(5), 80. <http://dx.doi.org/10.1007/s38313-019-0040-1>.
- Pischinger, M., Salber, W., van der Staay, F., Baumgarten, H., & Kemper, H. (2000). Benefits of the electromechanical valve train in vehicle operation. *SAE Transactions*, 109, 1414–1424, URL <http://www.jstor.org/stable/44634314>.
- Popp, T., Lechner, R., Becker, M., Hebauer, M., O'Connell, N., & Brautsch, M. (2019). Potentials of OME/Diesel blends for stationary power production – Improving emission characteristics of a Diesel CHP unit. *Applied Thermal Engineering*, 153, 483–492. <http://dx.doi.org/10.1016/j.applthermaleng.2019.03.015>.
- Postlethwaite, I. (1996). *Multivariable feedback control: Analysis and design*. USA: John Wiley and Sons, Inc.
- Putrasari, Y., & Lim, O. (2021). Dimethyl ether as the next generation fuel to control nitrogen oxides and particulate matter emissions from internal combustion engines: A review. *ACS Omega*, 7(1), 32–37. <http://dx.doi.org/10.1021/acsomega.1c03885>.
- Ritzmann, J., Zsiga, N., Peterhans, C., & Onder, C. (2020). A control strategy for cylinder deactivation. *Control Engineering Practice*, 103, Article 104566. <http://dx.doi.org/10.1016/j.conengprac.2020.104566>.
- Saputo, J. C., Smith, G. M., Lee, H., Sampath, S., Gingrich, E., & Tess, M. (2020). Thermal swing evaluation of thermal barrier coatings for diesel engines. *Journal of Thermal Spray Technology*, 29(8), 1943–1957. <http://dx.doi.org/10.1007/s11666-020-01117-3>.
- Sarıkoç, S. (2021). Effect of H<sub>2</sub> addition to methanol-gasoline blend on an SI engine at various lambda values and engine loads: A case of performance, combustion, and emission characteristics. *Fuel*, 297, Article 120732. <http://dx.doi.org/10.1016/j.fuel.2021.120732>.
- Schechter, M. M., & Levin, M. B. (1996). Camless engine. In *SAE technical paper series*. SAE International, <http://dx.doi.org/10.4271/960581>.
- Schemme, S., Breuer, J. L., Köller, M., Meschede, S., Walman, F., Samsun, R. C., et al. (2020). H<sub>2</sub>-based synthetic fuels: A techno-economic comparison of alcohol, ether and hydrocarbon production. *International Journal of Hydrocarbon Engineering*, 45(8), 5395–5414. <http://dx.doi.org/10.1016/j.ijhydene.2019.05.028>.
- scikit documentation page of MLPRegressor. (2022). [https://scikit-learn.org/stable/modules/generated/sklearn.neural\\_network.MLPRegressor.html](https://scikit-learn.org/stable/modules/generated/sklearn.neural_network.MLPRegressor.html). (Accessed 16 November 2022).
- Shadidi, B., Najafi, G., & Yusaf, T. (2021). A review of hydrogen as a fuel in internal combustion engines. *Energies*, 14(19), 6209. <http://dx.doi.org/10.3390/en14196209>.
- Soltic, P., Hilfiker, T., & Hänggi, S. (2019). Efficient light-duty engine using turbulent jet ignition of lean methane mixtures. *International Journal of Engine Research*, 22(4), 1301–1311. <http://dx.doi.org/10.1177/1468087419889833>.
- Song, C. H., & Aldering, L. J. (2019). Strategic intentions to the diffusion of electric mobility paradigm: The case of internal combustion engine vehicle. *Journal of Cleaner Production*, 230, 898–909. <http://dx.doi.org/10.1016/j.jclepro.2019.05.126>.
- Stepien, Z. (2021). A comprehensive overview of hydrogen-fueled internal combustion engines: Achievements and future challenges. *Energies*, 14(20), 6504. <http://dx.doi.org/10.3390/en14206504>.
- Tchetchik, A., Zvi, L. I., Kaplan, S., & Blass, V. (2020). The joint effects of driving hedonism and trialability on the choice between internal combustion engine, hybrid, and electric vehicles. *Technological Forecasting and Social Change*, 151, Article 119815. <http://dx.doi.org/10.1016/j.techfore.2019.119815>.
- Towaju, O. A. (2021). Fuels for automobiles: The sustainable future. *Journal of Energy Research and Reviews*, 8–13. <http://dx.doi.org/10.9734/jenrr/2021/v7i330191>.
- Unger, H., Schwarz, C., Schneider, J., & Koch, K.-F. (2008). The valvetronic. *MTZ Worldwide*, 69(7–8), 30–37. <http://dx.doi.org/10.1007/bf03227902>.
- Usman, A., & Park, C. W. (2016). Optimizing the tribological performance of textured piston ring-liner contact for reduced frictional losses in SI engine: Warm operating conditions. *Tribology International*, 99, 224–236. <http://dx.doi.org/10.1016/j.triboint.2016.03.030>.
- Verhelst, S., Turner, J. W., Sileghem, L., & Vancoillie, J. (2019). Methanol as a fuel for internal combustion engines. *Progress in Energy and Combustion Science*, 70, 43–88. <http://dx.doi.org/10.1016/j.pecs.2018.10.001>.
- Xia, F., Griefnow, P., Tidau, F., Jakoby, M., Klein, S., & Andert, J. (2020). Electric torque assist and supercharging of a downsized gasoline engine in a 48V mild hybrid powertrain. *Proceedings of the Institution of Mechanical Engineers, Part D (Journal of Automobile Engineering)*, 235(5), 1245–1255. <http://dx.doi.org/10.1177/0954407020968956>.
- Xue, X., & Rutledge, J. (2017). Potentials of electrical assist and variable geometry turbocharging system for heavy-duty Diesel engine downsizing. In *SAE technical paper series*. SAE International, <http://dx.doi.org/10.4271/2017-01-1035>.
- Yang, Z., Winward, E., Mason, B., Corre, S. L., Childs, T., & Shahzad, A. (2019). Nonlinear model predictive control of a variable valve timing system in a turbocharged spark ignition engine. In *2019 American control conference*. IEEE, <http://dx.doi.org/10.23919/acc.2019.8814687>.
- Yin, L., Turesson, G., Tunestal, P., & Johansson, R. (2020). Model predictive control of an advanced multiple cylinder engine with partially premixed combustion concept. *IEEE/ASME Transactions on Mechatronics*, 25(2), 804–814. <http://dx.doi.org/10.1109/tmech.2020.2969853>.
- Zhao, J., Xi, Q., Wang, S., & Wang, S. (2018). Improving the partial-load fuel economy of 4-cylinder SI engines by combining variable valve timing and cylinder-deactivation through double intake manifolds. *Applied Thermal Engineering*, 141, 245–256. <http://dx.doi.org/10.1016/j.applthermaleng.2018.05.087>.
- Zhu, S., Hu, B., Akehurst, S., Copeland, C., Lewis, A., Yuan, H., et al. (2019). A review of water injection applied on the internal combustion engine. *Energy Conversion and Management*, 184, 139–158. <http://dx.doi.org/10.1016/j.enconman.2019.01.042>.
- Zsiga, N., Omanovic, A., Soltic, P., & Schneider, W. (2019a). Functionality and potential of a new electrohydraulic valve train. *MTZ Worldwide*, 80(9), 18–27. <http://dx.doi.org/10.1007/s38313-019-0086-0>.
- Zsiga, N., Omanovic, A., Soltic, P., & Schneider, W. (2019b). Wirkungsgradvorteile beim Ottomotor unter Verwendung einer nockenwellenlosen, vollvariablen Ventilsteuerung gegenüber gedrosseltem Betrieb. In *VDI-Fachtagung Ventiltrieb Und Zylinderkopf*. Würzburg: VDI.
- Zurbriggen, F., Hutter, R., & Onder, C. (2016). Diesel-minimal combustion control of a natural gas-Diesel engine. *Energies*, 9(1), 58. <http://dx.doi.org/10.3390/en9010058>.